VALIDATION OF A 1D ALGORITHM THAT MEASURES PULSE WAVE VELOCITY TO ESTIMATE COMPLIANCE IN BLOOD VESSELS

A Thesis

presented to

the Faculty of California Polytechnic State University,

San Luis Obispo

In Partial Fulfillment

of the Requirements for the Degree

Master of Science in Biomedical Engineering

by

James Leung

June 2018

COMMITTEE MEMBERSHIP

TITLE: Validation of a 1D Algorithm that Measures Pulse Wave Velocity to Estimate Compliance in Blood Vessels

AUTHOR: James Leung

DATE SUBMITTED: June 2018

COMMITTEE CHAIR: Robert Crockett, Ph.D.
Department Chair of Biomedical Engineering

COMMITTEE MEMBER: Lily Laiho, Ph.D.
Professor of Biomedical Engineering

COMMITTEE MEMBER: Robert Szlavik, Ph.D.
Professor of Biomedical Engineering

ABSTRACT

Validation of a 1D Algorithm that Measures Pulse Wave Velocity to Estimate Compliance in Blood Vessels

James Leung

The purpose of this research is to determine if it is possible to validate the new 1D method for measuring pulse wave velocity in the aorta *in vivo* and estimate compliance. Arterial pressure and blood flow characterize the traveling of blood from the heart to the arterial system and have played a significant role in the evaluation of cardiovascular diseases. Blood vessel distensibility can give some information on the evolution of cardiovascular disease. A patient's aorta cannot be explanted to measure compliance; therefore we are using a flow phantom model to validate the 1D pulse wave velocity technique to estimate compliance.

Keywords: arterial system, cardiovascular system, electrical analog network model, flow phantom, Fourier-velocity encoding, general electric, mechanical testing, magnetic resonance imaging, MRI, phase contrast method, post analysis, pulse wave velocity, Siemens, uniaxial stretch testing,

ACKNOWLEDGEMENTS

I am grateful for my advisor, Dr. Robert Crockett, for his continuous advice, generous guidance and support that made it possible for me to work on a topic was both interesting and challenging for me. It was a pleasure and an honor to work with him.

I am hugely indebted to Dr. Gabriel Acevedo-Bolton for finding time to reply to my emails, for giving his advice regarding the writing of this thesis, and for helping me understand the work that was performed.

I am hugely indebted to Dr. David Saloner for giving me the opportunity to take on this research project when every other research project was dropped due to loss of funding during the 2008-2009 recession. I am grateful for his immense interest in my topic of research, for providing me materials and links that I could not possibly have discovered myself. His overview of nuclear physics and magnetic resonance imaging was significantly helpful to me.

I am grateful for Dr. Robert Szlavik for lending his time and electrical engineering expertise to guide my creation of electrical analog network model and for helping me make sense of my model.

I am grateful for Dr. Alison Meadows for helping me understand the potential applications of where my work can be relevant and useful.

I am grateful for Christopher J. Hardy in helping me understand the post-processing of the data using the 1D pencil excitation MRI method.

I am grateful for University of California, San Francisco and Veteran Affairs Medical Center, San Francisco for providing the facilities to perform my work.

TABLE OF CONTENTS

Page

LIST OF TABLES

LIST OF FIGURES

CHAPTER 1 INTRODUCTION

Arterial pressure and blood flow characterize the traveling of blood from the heart to the arterial system and have played a significant role in the evaluation of cardiovascular diseases. Blood vessel distensibility, defined as the relative change in vessel cross-sectional area over a pulse pressure, can give some information on the evolution of cardiovascular disease. For example, a stiff aorta provides an increased afterload on the heart while decreased distensibility of the aorta can lead to adverse consequences: (a) a loss of buffering in cardiac pressure pulsation, (b) an increase in the pulse wave velocity leads, (c) a higher pulse pressure, (d) an increase in the major risk factor in coronary artery disease, and (e) a decrease in diastolic pressure. A patient's aorta cannot be explanted to measure compliance; therefore we are using a flow phantom model to validate the 1D pulse wave velocity technique to estimate compliance. The question of interest is as follows:

> *Is it possible to validate the new 1D method for measuring pulse wave velocity in the aorta in vivo and estimate compliance?*

This work includes three (3) distinct projects, described below with the respective importance of each:

1. Measure and compare compliance values of tubes and MRI estimates using 1D method. Design model with segments including varying compliance values. *Importance: Validate if the compliance values of the tubing from the MRI estimates using 1D method is comparable to the compliance values of the tubing from mechanical testing methods.*

2. Check if 1D method can differentiate the different contributions to global compliance as a function of segment length. *Importance: Discern if flow phantom as a research test bench will enhance the understanding of flow patterns with a specific geometry. Discern if flow phantom model is sensitive enough to differentiate tubing with various compliances.*
3. Build analog electrical network model using estimated values from experimental measurements. *Importance: In vivo experimental studies used to study the effects of cardiovascular disease on arterial perfusion and peripheral pulse formation are both challenging and expensive to conduct and are limited to the easily accessible arteries. Consequently, the use of a computer model of the circulation offers an attractive alternative.*

CHAPTER 2 BACKGROUND

CARDIOVASCULAR SYSTEM AND ARTERIAL SYSTEM

The heart is the pump of the human circulatory system. The left side of the heart has two connected chambers: the left atrium and the left ventricle. Likewise, the right side of the heart has two connected chambers: the right atrium and the right ventricle. These two sides of the heart are not directly connected with one another. Oxygenated blood from the lungs travels through large vessels called pulmonary veins. It enters the left side of the heart and empties directly into the left atrium. The pulmonary veins are unusual in that they carry oxygenated blood; other veins carry deoxygenated blood because they carry blood back to the heart from the body tissues. From the left atrium, blood flows into the left ventricle through a one-way valve, called the left atrioventricular valve (also known as the bicuspid valve). Most of this flow — roughly 70% — occurs while the heart is relaxed. The atrium then contracts, filling the remaining 30% of the ventricle with its blood. After a slight delay, the ventricle contracts, forcing the blood to exit into an opening that leads to the largest artery in the body— the aorta. The atrioventricular valve closes and prevents the backflow of blood into the atrium. The aorta is closed off from the left ventricle by a one-way valve— the aortic semilunar valve. It is oriented to permit the flow of the blood out of the ventricle, but it snaps shut in response to backflow.

Accordingly, many arteries branch from the aorta, carrying oxygen-rich blood to all parts of the body. The pathway of blood vessels to the body regions and

organs other than the lungs is called systemic circulation. Systemic circulation brings blood to the neck and heart and to organs in the rest of the body. Moreover, systemic circulation gives up oxygen into the body tissues and receives carbon dioxide. The blood that flows into the arterial system eventually returns to the heart after flowing through the capillaries. As it returns, blood passes through a series of veins, ultimately entering the right side of the heart. Two large veins collect blood from the systemic circulation. The superior vena cava drains the upper body, while the inferior vena cava drains the lower body. These veins dump deoxygenated blood into the right atrium. Blood passes from the atrium into the right ventricle through a one-way valve, the right atrioventricular valve (also known as the tricuspid valve). Blood passes out of the contracting right ventricle through a second valve (the pulmonary semilunar valve) into a single pulmonary artery (the pulmonary trunk) which subsequently branches into arteries that carry deoxygenated blood to the lungs. The blood then returns from the lungs to the left side of the heart, replenished with oxygen and cleared of much of its carbon dioxide load. The pumping of the heart is a recurrent cardiac cycle of relaxation and contraction of the atria and the ventricles.

Naturally, some of the energy of left ventricular contraction produces forward blood flow during systole, but the majority is briefly stored as potential energy in the distended aorta. During diastole, this energy is then reconverted into forward blood flow as the aorta contracts [1, 2]. The purpose is to reduce the load on the

left ventricle of the heart, promote coronary artery perfusion, and maintain forward flow to the peripheral vascular beds[3].

In fact, there are several components of the vessel wall having different elastic properties, with elastin determining compliance at low pressures and with fully stretched collagen fibers determining higher stiffness at high pressures [4]. As a result, arterial pressure and blood flow pulses that result from the interaction of the heart and the arterial system have been an important determinant in the assessment of cardiovascular diseases. In fact, the amplitude and the shape of arterial pulses are strongly related to the peripheral circulation and cardiac function. Furthermore, input impedance of systemic circulation reveals the physical state of the vascular properties. [5].

In general, study of arterial hemodynamics involves the analysis of pressure and flow waveforms, since these are the fundamental quantities that characterize the propagation of blood from the heart to the peripheral vascular beds. Pressure and flow waveforms are continuously altered as blood flows from the aorta to the peripheral arteries. At any given arterial location, the shapes of these waveforms are determined by the properties of the cardiovascular system which include geometry, wall elasticity, peripheral impedances, heart rate, cardiac output, etc. Variation in the properties of the arterial system is exhibited by changes in the pressure and flow waveforms and in the presence of arterial disease such as arterial and aortic stenosis. These changes are overwhelmingly enough to carry

significant diagnostic value [6].However, simple observation is not enough. When some pathological modification is produced, measurement of significant parameters and establishment of a model to assess interrelations is observed to predict mass flow distribution [7].

DISEASE AND THE CARDIOVASCULAR SYSTEM

In recent years, a significant amount of attention has been focused on the pharmacological manipulation of the systemic circulation for cardiovascular disease such as hypertension, mitral and aortic valve regurgitation, and the congestive cardiomyopathies [8-10]. Surely, measurement of blood vessel stiffness is an important determinant of the evolution of cardiovascular disease (i.e., a stiff aorta provides an increased afterload on the heart).

The decrease in compliance of the aorta leads to a number of adverse consequences. A loss of buffering in cardiac pressure pulsation leads to elevated systolic pressure and reduced diastolic pressure. An increase in the pulse wave velocity leads to the early arrival of reflected pressure waves in end-systole, adding to the peak pressure and reduction of forward blood flow. A higher pulse pressure can in turn lead to an increase in ventricular loading [11, 12], and hypertrophy increasing the already major risk factor in coronary artery disease [13]. In addition, the decreased diastolic pressure leads to a reduction in coronary perfusion [3].

DISEASE AND PATIENTS

Reduction of aortic compliance has been found to correlate with age [14-16]and with pathological states, such as coronary artery disease [15-18], hypertension [19-23], heart failure [24, 25], and connective tissue disorders, including Marfan syndrome [26-31]. Hence, determination of the compliance could help design improved repair techniques in children with congenital heart disease since current commonly used methods often fail when the child reaches twenty to thirty years of age.

INDUSTRIAL SIGNIFICANCE

Many experimental studies have been performed to study the effects of cardiovascular disease on arterial perfusion and peripheral pulse formation. The major drawback of these *in vivo* studies is that they are challenging and expensive to conduct and are limited to the easily accessible arteries. Consequently, the use of a computer model of the circulation offers an attractive alternative [32-40].

Models are a simplification of reality which helps to understand function. A large majority of the computer models are based on the same set of governing equations, more specifically, the integrated, one-dimensional continuity and momentum equations. The existence of the differences between the various models is attributed mainly to the types of boundary conditions used, the nature of the vessel pressure-area relationship used, whether they are linear or

nonlinear, and the method of solution [6]. Previously developed models were intended to model the whole systemic circulation [33, 35, 38], whereas other models focused on parts of the arterial system [40, 41].

Obviously, to assess the ability of the models to accurately simulate arterial flow, model predictions are compared with experimental findings. Arterial compliance is usually determined either directly by measuring the change in vessel cross-sectional area and blood pressure over the cardiac cycle or indirectly by measurement of the pulse wave velocity along the vessel. The former method has been implemented with use of ultrasound [41] or cine X-ray angiography [42] and the latter with Doppler ultrasound [43], arterial applanation tonometry [44, 45], or micromanometers on catheters [46].

However, application of ultrasound methods to the aorta suffers from narrow acoustic windows and ability to achieve accurate spatial registration between different measurements. Applanation tonometry is not applicable to the central vasculature, projective X-ray techniques do not give accurate vessel cross sectional images, and catheterization is invasive [3].

The consideration of all these factors results in the determination of arterial elasticity using magnetic resonance imaging as the better alternative, since MRI is a painless, harmless investigation and may be repeated at will. . Studies in

normal subjects and in patients with cardiovascular disease have documented the clinical relevance of the method.

During clinical exploration, the present work will therefore extend the area of research to explain observations and to confirm inferences established. The MRI algorithm developed allows the quantification of the flow pulse in the compliant tubing with the assistance of previous mathematical models, enabling the possibility of measuring flow pulse in direction and magnitude in the tubing [7].

INVASIVE TECHNIQUES AND OTHER NON-INVASIVE TECHNIQUES

A number of non-invasive techniques, such as Doppler ultrasound and angiography, are used by surgeons to determine admittance for surgery. But these techniques alone are not adequate due to the special resolution and the quality of the imaging, leaving the surgeon to interpret the collected data without strong evidence or specific concrete data that supports the surgeon's decision. Therefore, a surgeon must rely on experience and expertise, or gut-feeling, to determine the sole decision of whether the patient will be admitted for surgery. The purpose of this study is to provide surgeons and clinicians with a more concrete set of acquired data that will help them determine if a patient should go into surgery [47].

MRI ALGORITHMS

Recent advancement of nuclear magnetic resonance imaging (nMRI) has led to an increased interest in vascular imaging for the study of arterial disease related

to cardiovascular disease [48-51]. Although MRI is well suited to provide three-dimensional geometrical information of arterial structure, it is generally too slow to provide complete hemodynamic data over an extended region of interest. For this reason, there is a growing trend to use geometrical data acquired by MRI to guide computational fluid dynamic (CFD) calculations of blood flow [52, 53]. In addition, for the suitability for real-time decision making in clinics, the models developed must contain a well-developed and fast algorithm [54].

DIRECT MEASUREMENTS METHODS

Number of related metrics for arterial elasticity is given by the stiffness index or β-index [41, 55] given as

$$\beta = \frac{\ln(P_s / P_d)}{(d_s - d_d)/d_d}, \tag{1}$$

where P_s and P_d are systolic and diastolic pressures, respectively, and d_s and d_d are the corresponding systolic and diastolic vessel diameters.

Local compliance [15] RC is expressed as the change in the regional vessel volume over the unit change in pressure

$$RC = L(A_s - A_d)/(P_s - P_d), \tag{2}$$

where A_s and A_d are the local systolic and diastolic arterial cross-sectional areas, respectively, and L is the chosen length of vessel (e.g., 1 cm).

Direct measurement of elasticity is the distensibility [56] *D*, which is expressed as the change in vessel cross-sectional area over pulse pressure:

$$D = \frac{(A_s - A_d)}{A_d\ (P_s - P_d)}. \quad (3)$$

Due to the change in the size and shape of the a representative lumen over the cardiac cycle, direct measurements are preferred in comparisons from the diameter [57].

And so, the metrics used consider the overall regional stiffness of the artery as tubing. The relationship of the elastic material property of the arterial wall, the ratio of wall thickness *h* to vessel diameter d_d can be incorporated *(56)* to yield the incremental Young's modulus *E*:

$$E = \frac{1}{D(h/d_d)} = \frac{(P_s - P_d)\ d_d^2}{(d_s - d_d)\ 2h}. \quad (4)$$

Assumption of the wall behaving as a thin, homogenous membrane is embraced. Consequently, accuracy is the limitation of any *in vivo* determination of Young's modulus by how precise *h* can be measured. Limitations to direct measurement methodology of aortic compliance are that they require the knowledge of the regional pulse pressure in the artery. For central vasculature, invasive determination requires intravascular pressure transducer or estimations from remote sphygmomanometer measurements, which usually overestimate central pressures in adult humans significantly [58].

FLUID PHANTOM MODELING

The driving factor to produce complex human arterial models is driven by a few goals, a major one being able to develop a research test bench that will enhance the understanding of flow patterns with a specific geometry, both one-dimensional and three-dimensional. This method has been used in previous studies in the development and progression of vascular disease: (a) research of the principle factor that regulates vascular structure under normal physiological anatomical conditions; (b) vascular flow phantoms are used throughout the development and testing of flow-linked imaging software systems; and (c) throughout the development process, realistic physiological conditions must be assessed and integrated into the development process which include the geometric accuracy, the necessary spatial resolution, and the presence of possible artifacts.

Advantageous models include animal models since they provide data such as vascular pulsatility, respiratory motion, cardiac motion, and other physiologic parameters. However, not every animal is the same, just as not every human is the same, leading to relative truth, thus absolute truth is not known. The data acquired does not assure the specific conditions relevant to human experimental data such as pulsatile flow waveforms and specific vascular geometries. Additionally, the generation of a reasonable approximation of a specific disease state of interest in laboratory animals is not always guaranteed a good representation. Thus, the use of anatomy accuracy to produce a flow phantom

providing a test setup which can be easily modified proves to be the most practical [59].

PREVIOUS MECHANICAL STRETCH TESTING

The purpose of the following previous study was to determine stiffness across a wide range of strain and nonlinear material properties of corresponding regions of native aortic roots. The inherent material properties in aortic roots were unknown, so aortic arterial tissue specimen from porcine aortic roots were subjected to displacement-controlled equibiaxial stretch testing below (15% strain), within (30% strain), and beyond (50% strain) physiological ranges to understand specific physiologic conditions. The results showed a relative stiffness in the aortic artery through the majority of the strain range. Thus, these inherent mechanical properties are important for understanding physiologic aortic root function [60].

ELECTRICAL NETWORK MODELING

Numerous models have been developed with the aim of attaining better insight and understanding of the relationship between physical phenomena occurring within the human aorta, such as pressure and flow wave transmission, and the properties of the aorta itself, such as radius, wall thickness, distensibility, and stiffness. As a result, three classes of models may be divided as the following: (a) simple mathematical models that can be studied using pen and paper, (b)

complex models requiring the use of digital software, and (c) physical models utilizing hydrodynamic or electrical analogs [33].

As of January 1997, numerous models have been proposed to simulate human arterial circulation from simple to complex [61-66]. The desire for attaining accurate data made it into *in vivo* measurements in canine in some pathological cases [7]. These models are based on electromechanical analogs, including a hydraulic transmission system of compliant tubing and an electrical transmission line, able to provide prediction of blood pressure and flow waveforms, provided with initial conditions of mechanical properties and parameters of the dimensions of the arterial system [67].

Nonetheless, the model has a limited clinical application due to its lack of autoregulation and dynamic response [54]. In an original “windkessel” model [68], the aortic artery acts as an elastic chamber in which diastolic pressure decays exponentially with a determined time constant, driven by total resistance and total capacitance. Later, refinements and additions for the accuracy of the model include the addition of inductance to represent blood inertia and for the division of arterial branching into smaller Windkessel elements in analog to a electrical transmission line model [69, 70].

Furthermore, the arterial system has been modeled in many other ways: lumped models [71, 72], tube models [73-75] and anatomically based distributed models

[6, 33, 76]. The first to measure blood pressure and to notice that the pressure throughout the arterial system varied over the heart beat was Hales in 1735. He suggested that the variations in pressure waveforms were correlated to the elasticity of the large arteries, namely, the aorta [77]. Historically, the first to propose the comparison of volume elasticity of larger arteries with the Windkessel presentation in fire engines (Figure2.0) was Weber (Weber EH (1827) as cited by Wetterer and Kenner [75]. Later, Frank [71] quantitatively devised and popularized the two-element Windkessel model which consisted of a resistance and capacitance element. According to Poiseuille's law, the resistance is inversely proportional to blood vessel radius to the fourth power. Overall resistance to flow in the global arterial system is mainly found in the resistance of the small arteries and the arterioles. The summation of the total peripheral resistance includes the resistance of the entire systemic vascular bed and is calculated by the addition of all individual resistances in the microcirculation. The peripheral resistance, R, is calculated as:

$$R = \left(P_{ao,mean} - P_{ven,mean}\right)/CO \approx P_{ao,mean}/CO \quad (5)$$

with $P_{ao,\,mean}$ and $P_{ven,\,mean}$ mean aortic and venous pressure and CO cardiac output. [77].

Overall capacitance is mainly determined by the elasticity of the large or intermediate arteries. The summation of the total arterial compliance is calculated by the addition of the compliances of the entire arterial system. The

total arterial compliance, C, is the ratio of the change in volume, ΔV, and the resultant change in pressure ΔP:

$$C = \Delta V / \Delta P \tag{6}$$

Conversely, there is difficulty in performing an experiment where volume injection into the arterial system will not result in a volume loss down the periphery. Therefore, a few methods to obtain total arterial compliance were developed, and the ones based on the Windkessel are discussed.

When the aortic valve is closed at end-systole, the two-element Windkessel model predicts that in diastole, pressure waveforms will decay exponentially given a characteristic decay time RC. In a previous study, Frank's objective was to obtain cardiac output. He concluded that with the characteristic decay time RC when derived from the aortic pressure at end-systole (in diastole), an independent initial condition estimate of total arterial capacitance would calculate the total peripheral resistance.

Therefore, the cardiac output is the average velocity of blood flow which is simply the change in aortic pressure divided by the regional peripheral resistance. Frank can then predict total arterial compliance from pulse wave velocity waveforms in the aorta. From this example, due to resistive and capacitance relationships, complementary information can be estimated using the Windkessel models and wave transmission of pressure in the aorta [77].

Surely, the Windkessel is also known as a lumped model. This lumped model entails the entire arterial system, in terms of a pressure-flow relation at its entrance, by the two elements that represent the physiologic. The research of pressure waveforms, flow wave propagation and reflected waves is a phenomenon that cannot be studied because they are inside the arterial tree.

In previous hypertension research, an important note to consider is that they focused mainly on peripheral resistance and neglected the contribution of total arterial compliance to blood pressure. (The groups of Safar [78] and Westerhof [79] were exceptions in this respect, Figure 2.1).

More recent research in 1997 showed that pulse pressure is a critical predictor of cardiovascular morbidity and mortality [80, 81]. A conclusion researchers made was the realization that arterial compliance is also a great significance, especially in old age (systolic) hypertension. From the two-element Windkessel model, the load of the left ventricle of the heart consists of peripheral resistance and total arterial compliance which contribute to significance in diagnostics.

NEED FOR NON-INVASIVE MRI

INDIRECT MEASUREMENTS METHOD

An alternative, indirect method for determining arterial compliance is measuring the pulse wave velocity $V_{pw.}$ This methodavoids the previous problem of requiring knowledge of regional pulse pressure and needing invasive methods to

determine pressure estimations, usually encountering estimations. For any incompressible fluid in a rigid artery, pressure and flow waveforms changes would be transmitted down the vessel right away. However, for non-rigid arteries, the pressure pulse wave would distend the vessel and the flow waveform would travel along the artery at a finite velocity. According to the variant of the Moens-Korteweg equation [69], V_{pw} can be related to compliance:

$$D = 1/\left(\rho V_{pw}^2\right), \tag{7}$$

where the blood density ρ can be taken as constant at 1.057 ± 0.007 g cm^{-3} in normal subjects [82]and expected variations among patients are small.

Pulse wave velocity is calculated by the measurement of the time delay Δ*t* of the flow waveforms between upstream and downstream locations knowing the relative separation Δ*s*. But, the measured wave velocity is increased by the blood flow inertia and thus can be corrected by subtracting the instantaneous blood velocity V_b at the point on the flow velocity waveform where the time measurement is made [69]:

$$V_{pw} = \frac{\Delta s}{Dt} - V_b. \tag{8}$$

Exceptionally, if the beginning foot of the velocity waveform is used as the reference point, then the blood flow velocity correction mentioned previously may be dropped:

$$V_{pw} = \frac{\Delta s}{\Delta t}. \quad (9)$$

Additionally, the use of the beginning foot of the velocity waveform is advantageous in that it avoids contributions of any reflection waves that arrive later.

Collectively, numerous nuclear magnetic resonance methods have been published for the determination of arterial compliance. These methods are categorized as direct methods determination by measuring the cross-sectional area changes and indirect methods determination by measuring the pulse wave velocity [3]. Clearly, there is a need for techniques to measure arterial compliance and MRI is the most promising way to achieve this. All this important work has been done, with MRI being the most promising, but there are gaps in our knowledge. The experiments described here seek to reduce these gaps.

MAGNETIC RESONANCE CROSS-SECTIONAL AREA

INDIRECT MEASUREMENTS DONE IN HISTORY

Some of the first few to perform magnetic resonance determination of aortic distensibility were Mohiaddin et al. [15, 17]. They acquired end-systolic and end-diastolic images perpendicular to the midpoints of the ascending aorta, the aortic arch, and the descending thoracic aorta using a spin echo pulse sequence. Manually, they outlined the lumen of the aorta and calculated the change in area

between systole and diastole. For normal subjects under 50 years of age, they found a mean change of 30% and a reproducibility of the measurements to be 6%. Applied use of this method measured arterial compliance of the pulmonary arteries in nine normal volunteers [83]. The average values, expressed as percentage change in cross-sectional area, were 25.6 ± 10.7 for the main pulmonary artery, 21.4 ± 10.7 for the right pulmonary artery, and 24.5 ± 7.8 for the left pulmonary artery.

Later studies included the use of cine gradient echo magnetic resonance imaging to perform measurements of aortic area over the cardiac cycle [57, 84]. In one study [84], they concluded that spin echo imaging provided excellent results when compared to gradient echo when optimization of spacial saturation pulses and flow compensation were used to enhance contrast between the aortic wall and lumen. In the other study [57], gradient echo imaging was better when low tip angles (20–30°)and higher spatial resolution (0.5–1.2 mm) were used in addition to signal thresholding employment before the outlining of the cross-sectional areas. The study notes that cine gradient echo is superior in being able to provide high-time resolution time sequences over the cardiac cycle, allowing the technician to choose the cardiac cycle phases and which vessel distension is minimized and maximized in each subject at end-diastole and end-systole, respectively.

Similarly, two more studies of aortic distensibility have been done, both performing an improved systematic analysis of spin echo [85] or gradient echo [86] techniques. In 47 healthy volunteers, the spin echo method [85] was used to measure short- and long-term reproducibility. The determination of long-term reproducibility in 24 subjects was 3 ± 7% (SE). On the other hand, short-term reproducibility in 15 subjects was determined to be 7 ± 6% and when modification of scan protocol by incorporation of two averages to improve spatial resolution, reproducibility improved to 2 ± 5%. When comparing the gradient echo method and the spin echo method, the gradient echo method had a 35% lower value of compliance than the spin echo method. The conclusion drawn was from the challenges in distinguishing the blood-wall boundary in their gradient echo technique.

In the other study, the cine gradient echo sequence and an automated snake-based edge detection algorithm were used to determine cross-sectional area to perform aortic compliance measurements. In addition to standard gradient echo imaging, a balanced steady-state free precession (SSFP) variant with a pulse wave velocity technique was used for comparison. Relative error was found in the measurement of compliance of 7% for both standard gradient echo and balanced SSFP methods. The results showed that the pulse wave velocity was more consistent with balanced SSFP (Pearson correlation coefficient of 0.94) than with the standard gradient echo (coefficient 0.88).

The authors believe it was because of the attribution of the improved blood–wall contrast of balanced SSFP when compared to the standard gradient-echo.
In 10 normal volunteers, the acquisition of black blood images of carotid arteries at end-systole, mid- to end-diastole was gathered by the use of a three-dimensional double-inversion fast spin echo pulse sequence with selective volume excitation [87].

The determination of compliance depended on the function of position along the carotid artery. In 10 subjects, relative changes in cross-sectional area ranged from 9-23% and the distensibility increase was found in the carotid bulb relative to the common carotid artery. The advantages of this method are that it can detect not only the distension of the lumen area along the vessel, but include changes in the geometry of arterial wall that may deviate from the circular lumen shape that occurs in many diseased vessels (i.e., calcification).

Most Recent Indirect Measurements

In Figure 2.0, a normal volunteer's measurement of aortic distensibility with the use of one variant of the area method is shown. First, acquisition of an oblique sagittal image was taken and then a plane was prescribed (line, Figure 2.0A) that is orthogonal to the aorta, at the level of the bifurcation of the pulmonary artery.

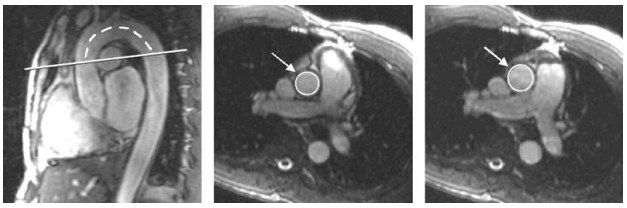

Figure 2.0 Normal volunteers measurement of aortic distensibility (**A**) Oblique sagittal view of aorta of normal volunteer, used to prescribe transverse slice (straight line) for balanced SSFP cine data sets of aorta. Vessel areas are then determined from contours (arrows) traced on end-diastolic (**B**) and end-systolic (**C**) time frames and used, along with pulse-pressure measurements, to determine vessel distensibility.

Next, the usage of cine imaging was performed using the balanced SSFP gradient echo pulse sequence to measure aortic area at end-diastole (Figure 2.0B) and end-systole (Figure 2.0C). Then, the regional pulse pressures were determined from the use of peripheral sphygmomanometric measurements. And finally, the compliance was determined from Eq. 3.

PHASE CONTRAST METHODS

Pulse wave velocity was measured using a cine gradient echo pulse sequence with and without bipolar gradients to encode through-plane blood velocity [16]. Cross sections of the mid-ascending and mid-descending thoracic aorta were included in the images and they were obtained as a function of time after the cardiac *R* wave in a plane orthogonal to the aorta at the level of the bifurcation of

the pulmonary artery. Instantaneous flow was determined from the average blood velocity and the aortic cross-sectional area.

Pulse wave velocity was determined from Eq. 9, where the transit time Δt was measured from the base of the flow wave in the mid-ascending and mid-descending aorta, and the distance between the two points Δs was determined by manually drawing a line along the center of the aorta in an oblique sagittal image. [3]

For that matter, modifications of this technique included the use of retrospective gating to avoid distortions and omittance of non-velocity-encoded reference to reduce imaging time [88]. By subtracting the phase data attained at the beginning of the cardiac cycle, where only small blood flow occurs, residual phase variations were removed. This allowed for the acquiring of two to three slices with a 3ms resolution time, summing measurement time to less than 11 minutes.

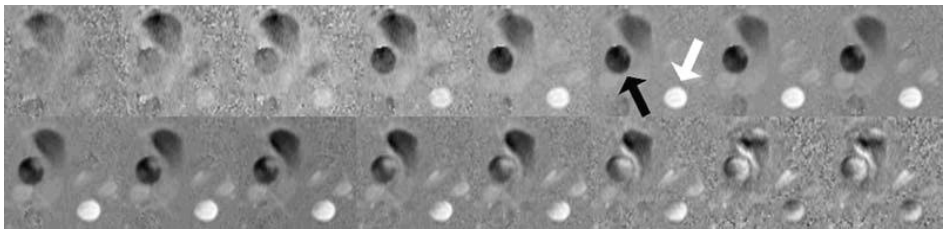

Figure 2.1. Selected time frames from cine phase contrast data set showing blood flow in ascending (e.g., black arrow) and descending (e.g., white arrow) aorta. Signal is integrated over vessel lumen for each time frame to determine net flow. Slices are from the same level prescribed in Figure 2.0A.

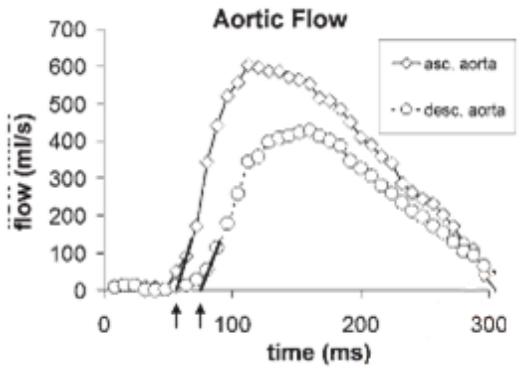

Figure 2.2. Plots of blood flow versus time in the ascending and descending aorta. Plots of blood flow vs time in the ascending (solid line, diamonds) and descending (dashed line, circles) aorta, taken from data set of Figure 2.1. Time delay (arrows) is measured from the foot of the flow wave in the two curves and divided by the distance between the vessel sections (curved line in Figure 2.0A).

In the determination of pulse wave velocity, there is some uncertainty related to the two-slice measurement and estimations are around 15% in a flow phantom

and higher in humans. Multislice oblique imaging with two-directional velocity encoding was applied with the aorta in plane to produce flow curves over 10 segments of the aorta. [89].

Figure 2.1, from the same plane prescribed in Figure 2.0A, is a series of time frames from a cine phase contrast data set attained from a normal volunteer. The ascending aortic flow is the region of cranial flow indicated by dark pixels (black arrow) and the descending aortic flow of caudal flow indicated by white pixels (white arrow). Accordingly, the integration of the signals over the area of the aortic lumen in each time frame yields velocity flow waveforms shown in Figure 2.2 for the ascending and descending aorta. The measurement of the time delay between the flow waves, taken at the foot of the base, can be divided by the distance between the positions along the midline of the aorta (Figure 2.0A) to determine pulse wave velocity.

An ECG-gated phase contrast pulse sequence was developed [90, 91] to increase spatial resolution and reduce scan times in which selection of one or more slices was replaced by the excitation of pencil-shaped regions [92, 93] (Figure 2.3) that run along the aorta. Second, a bipolar velocity-encoding pulse was applied followed by a readout gradient, both applied longitudinally to the pencil beam. Next, sequence was reiterated on the following electrocardiographic (ECG) trigger, with inverse polarity of the bipolar pulse, and finally taking a difference in the signals from the two acquisitions.

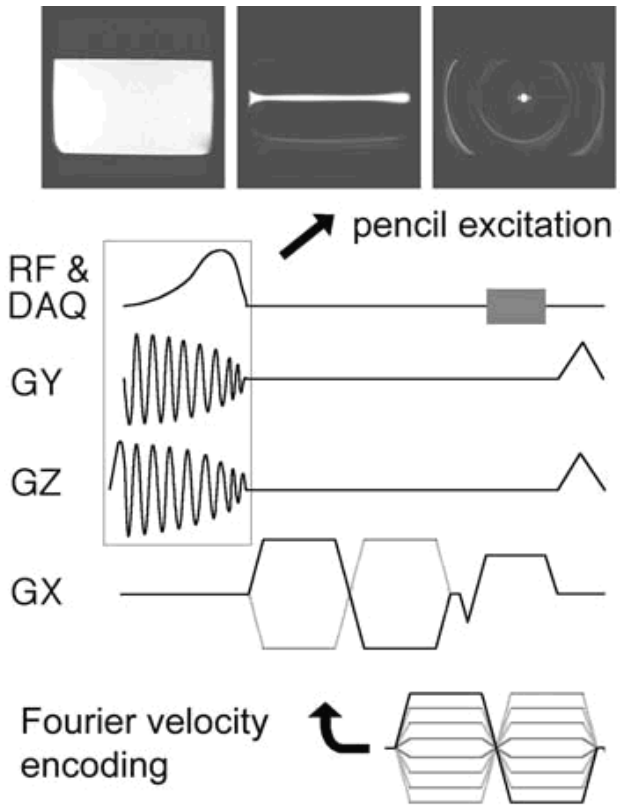

Figure 2.3. ECG-gated phase contrast pulse sequence versus Fourier-velocity encoding. Phase contrast MR M-mode pulse sequence used to measure aortic pulse wave velocity. Initial 2D-selective pulse excites pencil-shaped region shown at top (left: image of uniform phantom; center: side view of pencil; right: end view of pencil). In Fourier velocity-encoded variant (bottom), the bipolar gradient pulse is stepped through multiple levels instead of only two, and resulting data undergo Fourier transformation in the velocity-encoding dimension.

Repeating the sequence over multiple cardiac phases, with a resolution time of 20–30 ms, produces a scrolling display of position along the vessel vs time, where intensity of the images is proportional to blood velocity. Staggering the gating delay by 2-ms intervals and interleaving the results improves the effective resolution time, yielding a total scan time averaging 32 heartbeats. Lastly, the pulse velocity is the slope of the leading edge of the foot of the velocity trace.

FOURIER VELOCITY-ENCODING METHODS

Advantages of Fourier velocity encoding over phase contrast methods is the capability for the measurement of distribution of velocities within a voxel [94, 95], which improves the visualization of the flow wave as it travels down the artery. There has been integration of this feature in several pulse sequences, including one that integrates comb excitation of multiple slices into the Fourier velocity encoding [96]. In a study, five slices were simultaneously excited orthogonally to the femoral artery at 4-cm intervals. In the direction of the slice, Fourier velocity encoding was applied and the comb excitation pulse, designed to increment the phase of each slice by a different amount for each bipolar velocity-encoding pulse, was also applied which results in a velocity vs position plot in which the velocity spectra from assorted slices are stacked vertically in the velocity dimension. Repeating this sequence at multiple phases of the cardiac cycle resulted in a movie clip of blood velocities where the velocity waveform can be seen as traveling down the artery in from a slice to slice format. In this study, a

healthy 35 year old volunteer's distensibility in the femoral artery was calculated to be 1.7 x10^{-6} cm s^2/g.

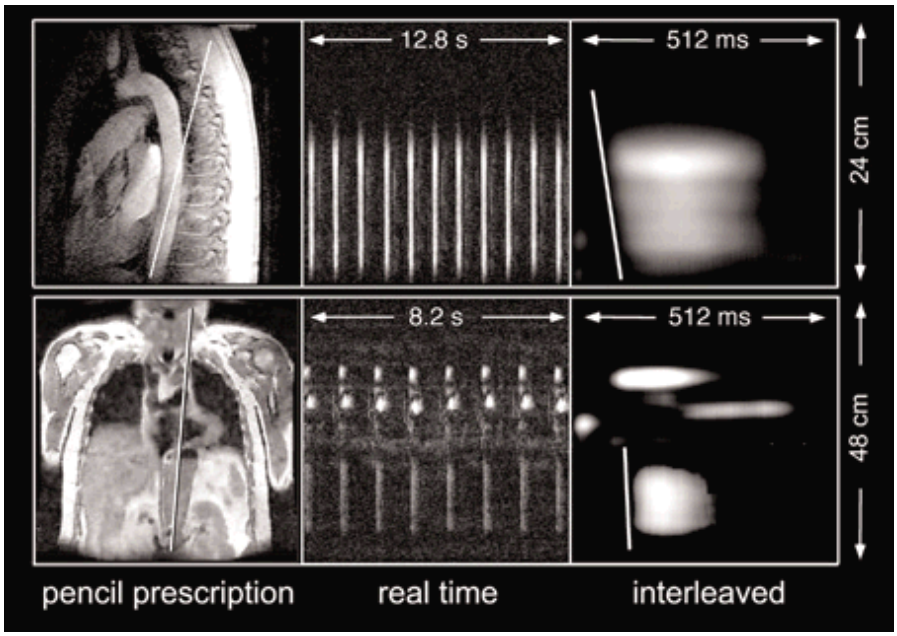

Figure 2.4. Phase contrast M-mode data sets of normal volunteer versus patient with aortic aneurysm. Phase contrast M-mode data sets from descending aortas of (top) normal volunteer and (bottom) patient with aortic aneurysm secondary to Marfan syndrome. Slope of leading edge of flow gives pulse wave velocity, which is 340 cm/s in normal volunteer (top right) and 1600 cm/s in Marfan patient (bottom right).

Similar to Doppler M-mode results, a different ECG-gated method integrated the pencil excitation with the Fourier velocity encoding method to produce movie clips of blood velocity distributions [97]. The pulse sequence was similar to a previous study [98], but instead the bipolar velocity encoding gradient was

stepped to a different value on each ECG trigger, usually through a total of 16 steps (Figure 2.3, bottom), and then the collected signals were “Fourier transformed to produce a velocity spectrum on the horizontal axis as a function of position along the pencil on the vertical axis" (Figure 2.5). In an effort to improve the resolution time to approximately 6ms, trigger delay was incremented by 4x, by 6 ms each time, and interleave the frames later. The results could then be displayed as a movie clip in which the velocity waveform can be seen as traveling across the frame. In any case, the location of the base of the foot of the velocity waveform in each frame is determined at the intersection point with the horizontal (zero-velocity) axis. Best fit analysis is then calculated from base-foot position vs time, and the pulse wave velocity is determined by the slope. The total scan time approximates to 64 heartbeats. Benefits of this integration of the pencil excitation with the Fourier velocity encoding method sheds light on blood flow details, which includes helical flow patterns that are in the thoracic aorta I and retrograde flow through diseased aortic valves.

SINGLE-HEARTBEAT METHODS

Many of the previous methods that use ECG-gated techniques may not be applicable in patients who have irregular heart rhythm because the methods can become degraded resulting in either ghosting or irregular motion of the velocity waveforms.

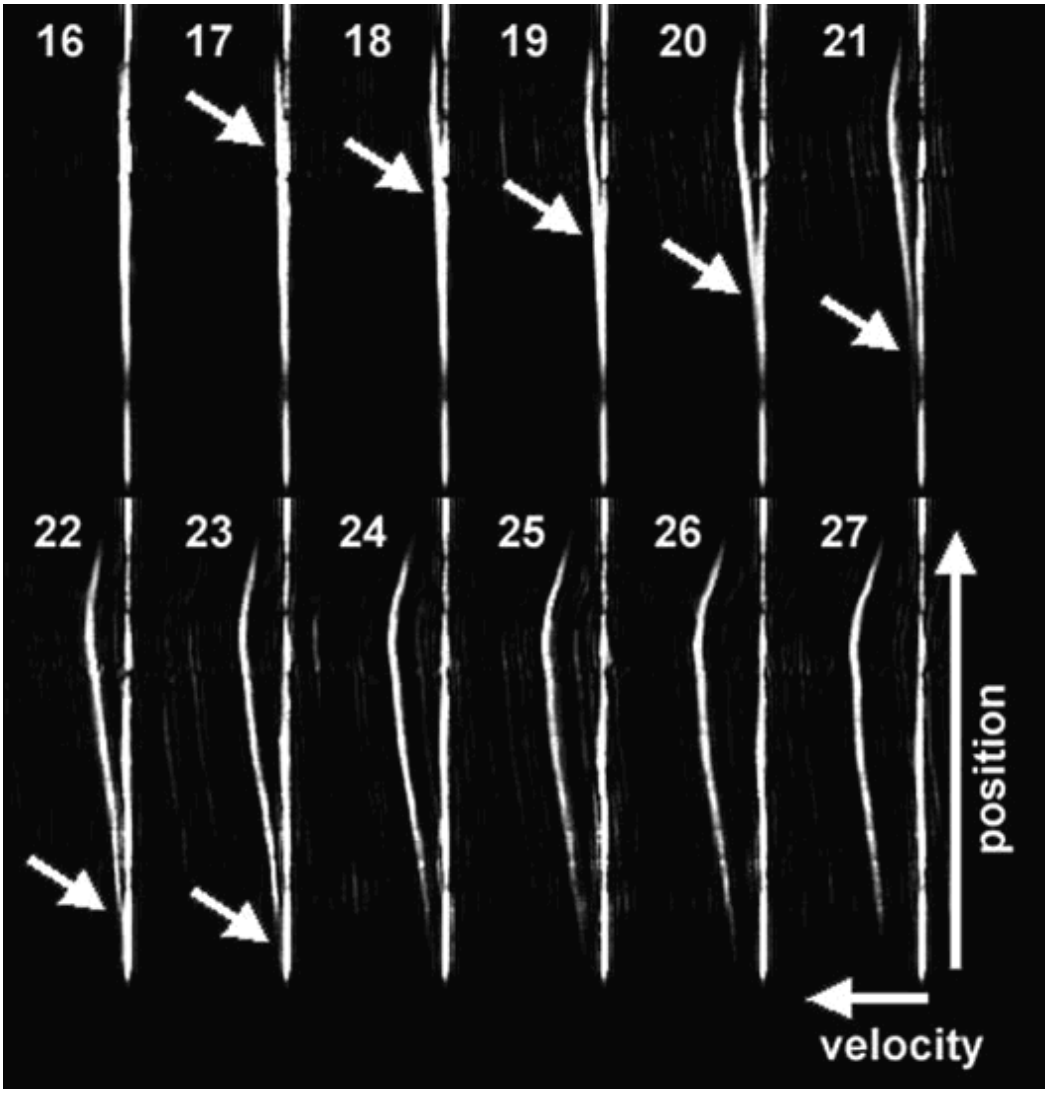

Figure 2.5. Velocity as a function of position along pencil. Frames 16–27 from Fourier velocity-encoded M-mode data set from descending aorta of normal volunteer, showing propagation of foot of flow wave (arrows) down the aorta. Field of view (vertical axis) was 240 cm zoomed to 190 cm; time per frame was 3.6 ms; wave velocity was 550 cm/s.

Several techniques have been developed that address the problem by acquiring flow wave velocity information within one heartbeat. One thing to keep a note of

is that these techniques often are used over a few heartbeats and averaged. Phase encoding was omitted to generate a real-time projective pulse sequence in one investigation [55]. The objective was to use a slice-selection gradient, orthogonal to the artery of investigation, and timing was adjusted in order to encode the flow velocity waveform in the slice direction into a phase shift. Pulse sequence mentioned was quickly interleaved between an upstream slice and a downstream slice to produce two side by side images of position vs time plots where systolic blood flow appears as white phase changes in the image of the artery. The contamination by contributions from static spins in the vessel signal is common, especially in the same project; consequently, a correction technique was developed and employed to subject the static stationary signals. The pulse wave velocity was then calculated from the difference in time in the base of the foot of the velocity wave between the two slices and the distance between them. In an experiment of 15 volunteers, the abdominal aorta pulsatile flow values averaged to be approximately 3-4m/s with an uncertainty of 0.6 m/s. The reduction of contaminated static tissue is, in part, in the usage of ECG-gated presaturation sequence that consists of repeated sinc-cos RF pulses in the presence of a rotating gradient field. The sequence produces an annular saturation region that has an unaffected central region that encompasses the aorta. Repeating the measurement portion of the pulse sequence continued which consisted of simultaneous excitation of an upstream and a downstream slice, orthogonal to the artery, and then followed by a readout along the slice-selection direction. The signal is a result of the projection where four distinct

peaks can be viewed with the corresponding static and moving spins from each of the upstream and downstream slices. Between each static and moving pair, the separated peaks were then used to calculate blood velocity in the corresponding slice at that specific point of time. Since the measurement sequence is repeated, a curve of blood velocity vs time can be plotted for each slice. Next, wave velocity was determined by measuring the separation between the midpoints of the rising waveforms and applying Eq. 6. In a study of 10 healthy volunteers, using the sequence mentioned, the average wave velocity in the thoracic aorta was 591 cm/s with a reproducibility of 7.6%.

When comparing this method and a more conventional phase velocity two-dimensional mapping technique, correlation was found to be R = 0.95. In order to reduce contamination of the blood signal by the adjacent static tissue, an alternative single-heartbeat projective technique [90] was used which was a dual-band saturation of the regions on either side of the aorta and followed by a 2D selective excitation of a column centered with the aorta. A spatial modulation of magnetization (SPAMM) tagging sequence was applied to sinusoidally modulate the signal down the axis of the aorta between saturation and excitation. A series of 128 first-moment-nulled gradient echoes was collected post-excitation. An image of the position along the aorta vs time is the result of the method where the flow waveform travel can be viewed as periodic white bands that initially start horizontal; however, the series tail down as the foot of the velocity wave reaches each band. The slope of the line connecting the inflection points of each band is

essentially the pulse wave velocity that is being measured. In a study of four healthy volunteers under 30 years of age, mean wave velocity was recorded as 4.2 m/s and the uncertainty was 0.5-0.9m/s. An effort to improve the spatial resolution in a related ECG-gated single-heartbeat method used a comb-excitation pulse to tag nine locations along the artery of experiment [91, 99]. After, a series of 64 gradient echoes sampled the signal at a 2-ms resolution time, in an attempt to reduce contamination from static signals; spatial pre-saturation to the posterior region of the aorta prior to excitation was applied. This method resulted in an image of position along the artery vs time, similar to that of the SPAMM method. The only difference was the narrower white bands. In five healthy volunteers ranging from 22-72 years of age, the pulse wave velocity ranged from 4.1 to 9.8 m/s and the measurement uncertainty from 0.5 to 1.1 m/s.

Indirect Methods

Numerous groups have developed indirect MR methods for the determination of pulse wave velocity. Groups tend to correlate the properties of the extended portions of the velocity flow waveform rather than the time of the motion of the foot of the waveform alone. For example, in performance of phase contrast velocity imaging of multiple sections of the aorta, then estimation of aortic compliance by correlation of second-order spatial and temporal derivatives of blood velocity, most of the cardiac cycle [100, 101] according to the equation

$$V_{pw} = \sqrt{\frac{\partial^2 V_b}{\partial t^2} \Big/ \frac{\partial^2 V_b}{\partial z^2}}. \quad (10)$$

[15] resulted in the accuracy of the method being 16% for vessels with compliance that exceeds 0.37% per mmHg with errors reaching 46% in more rigid arteries [100]. "Wave velocities between 360 and 473 cm/s were measured in three pigs [101], compared with values of 400–485 cm/s determined by timing the foot of the wave. Micromanometer measurements produced an average value that was 42 ± 35 cm/s higher than the values determined from Eq. 10."

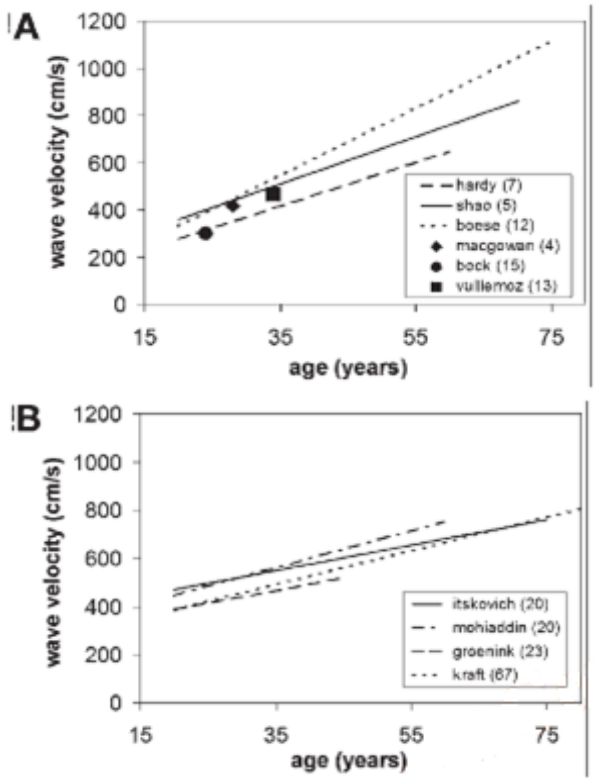

Figure 2.6. Aortic pulse wave velocity as a function of age. Plots of pulse wave velocity vs age in normal descending aorta, from MR studies with **(A)** fewer than 20 subjects and **(B)** 20 subjects or more. Study first authors and number of subjects are listed in keys.

To validate the micromanometer measurements, pressure waveforms were derived from the wave velocity measurements and changes in the cross-sectional area to compare. By using ECG-gated phase contrast imaging of a slice orthogonal to the ascending and descending regions of the aorta at relative location 5 cm distal of the aortic valve [102], aortic cross-sectional area was determined from the magnitude images, and the flow velocity waveforms was extracted from the phase images by summing the volumetric flow of each pixel

within the aorta where pulse wave velocity is calculated by plotting flow vs area over the cardiac cycle and averaging the slope of the line in beginning systole. "Thus,

$$V_{pw} = \Delta Q / \Delta A, \tag{11}$$

where ΔQ is the change in flow, and ΔA is the change in area. In 13 young healthy volunteers, mean wave velocity in the ascending aorta was 4.9 ± 1.1(SD) m/s compared to 4.4 ± 0.9 m/s using a foot-to-foot measurement and 6.7 ± 1.4 m/s using brachial pulse pressure measurement and Eqs. 3 and 5. [3]"

Paired *t*-test showed no significant difference with the foot-to-foot method and a highly significant difference with the brachial pressure method, with the latter discrepancy assigned to the use of brachial measurements to approximate aortic pressures. [3]

In Figure 2.6, aortic pulse wave velocity as a function of age as measured in 10 separate MR studies on normal volunteers is shown. Study by first author along with the number of subjects scanned in each case is displayed in the key. "Average values range from around 3–4 m/s in 20-yr-olds to 7–8 m/s in 70-yr-olds." The standard deviation in values within each age tertile (young, middle, aged) was averaged around 20% in normal subjects [99]. Equation 7 can be used to compare the pulse wave velocities in Figure 2.6 to aortic distensibility values. Thus, a pulse wave velocity of 4 m/s corresponds to a distensibility of 7.9

$x10^{-3}$ $mmHg^{-1}$, and a value of 8 m/s corresponds to a distensibility of 2.0 $x10^{-3}$ $mmHg^{-1}$.

CLINICAL STUDIES

Traditionally, MR have been used to measure aortic compliance in a number of different cardiovascular diseases, including hypertension [19-22], coronary artery disease [15, 18, 103], heart failure [24, 25], Marfan syndrome [27-31, 104, 105]and other related diseases [31]. A majority of the analyses utilized cine gradient echo imaging [18-22, 24-26, 28-31, 104] to determine systolic and diastolic cross-sectional areas. Additionally, one group used phase contrast magnetic resonance imaging to measure aortic pulse wave velocities [28, 30, 104] in patients with Marfan syndrome. In the majority of MR studies of hypertension, aortic compliance was significantly decreased [20-22], with, for 2.5 ± 0.4, 2.2 ± 0.4, 2.3 ± 0.4 $x10^{-3}$ $mmHg^{-1}$ vs 7.0 ± 1.6, 5.1 ± 0.3, 7.3 ± 0.8 x 10^{-3} $mmHg^{-1}$ in control subjects ($p < 0.05$) descending, and abdominal aorta, respectively[21].

The same study also found that systolic blood pressure ($R = -0.662$, $p = 0.000007$), left ventricular mass ($R = -0.484$, $p = 0.0067$), and abdominal visceral fat ($R = -0.416$, $p = 0.023$) were inversely related to aortic compliance, with intracellular free magnesium showing a positive correlation ($R = 0.712$, $p = 0.006$ in brain). In a study of pulmonary hypertension, fractional change in cross-sectional area of the pulmonary arteries was significantly reduced [23] from 23 to

8% ($p > 0.005$). Even though pulse pressure was not measured there is high probability that the pulse pressure is likely to be higher in patients which would reduce compliance further when compared to normal control patients. In two MR studies of patients with coronary artery disease [15, 18], significant reduction of aortic compliance was found (e.g., 2.9 ± 1.6 and 2.7 ± 1.1 $x10^{-3}$ $mmHg^{-1}$ in ascending and descending aortas, respectively, of patients vs 6.5 ± 3.1 and 4.5 ± 2.5 x 10^{-3} $mmHg^{-1}$, $p < 0.05$, in controls; *11*), noting in one of the studies this effect appeared to be most pronounced in patients under the age of 50 yr [15]. In a study, patients with risk factors for coronary atherosclerosis showed a high correlation of pulse pressure with pulse wave velocity, but not with plaque build-up in the aorta [103]. Area of aorta increased with the increase in plaque build-up suggesting that there may be aortic remodeling in this group.

In other MR studies, aortic compliance notably decreased in systolic [24] and diastolic [25] heart failure patients determined by the correlation with peak exercise oxygen consumption. Older volunteers (age ≥ 60 yr) with systolic heart failure, distensibility of the proximal aorta was 0.5 ± 0.4 $x10^{-3}$ $mmHg^{-1}$ vs 2.2 ±1.2 x 10^{-3} $mmHg^{-1}$ ($p < 0.002$)in normal subjects (age ≥60 yr) [24]. Aortic compliance was notably by the correlation of peak VO2 ($R = 0.80$, $p < 0.0001$), suggesting that an increase in aortic stiffness may be part of the cause of exercise intolerance in patients that have heart failure caused by left ventricular systolic dysfunction and in this way may serve as a therapeutic target for this disease. In MR studies of Marfan syndrome, there was found to be a decrease

in aortic distensibility in patients [26, 27, 29, 104, 105], with age not being a factor [26]. For example, Groenink et al. found compliance values of 3.0 ± 2.6, 3.4 ± 1.9, 5.1 ± 2.0, and 3.8 ± 2.2 x 10^{-3} $mmHg^{-1}$ at four various levels extending from ascending to abdominal aorta vs 4.4 ± 2.2, 4.6 ± 1.5, 5.4 ± 2.3, and 5.2 ± 3.4 x10^{-3} $mmHg^{-1}$ at the same levels in normal controls (with *p* values of 0.03, 0.01, >0.5, and 0.02, respectively) [104]. Similarly, pulse wave velocity measurements between the same levels in the same study showed increased values of 4.4 ± 1.1, 6.7 ± 2.2, and 5.5 ± 1.5 m/s vs 3.8 ± 0.7, 4.6 ± 0.9, and 4.5 ± 0.9 m/s in controls (p = 0.01, < 0.001, 0.003, respectively) in all regions of the aorta. Long-term research of 78 Marfan patients shows that the combined measurement of compliance and area had importance in the prediction of progressive dilatation of the aortic artery [30].

CONCLUSIONS

In large central arteries, more specifically the aorta, compliance serves to be a buffer to cardiac pressure pulsation and maintain forward blood flow to the peripheral vessels; at the same time reducing the afterload on the left ventricle and promoting coronary perfusion. The increase of stiffness of the aortic artery due to disease results in an increase in pulse pressure which may lead to long-term medical damage, cardiac pressure overload, and hypertrophy. MR technology provides a noninvasive yet accurate means to measure arterial distensibility and therefore may be a stepping stone in the assessment of cardiovascular risk and treatment monitoring. Of the MR methods for the

determination of arterial distensibility, the pulse-wave velocity method is superior when compared to the cross-sectional area method because it does not require the estimation of regional blood pressure. Even though numerous MR methods have been developed for the determination of pulse wave velocity, the gradient echo-based cine phase contrast pulse sequence is the most widely available, which can be used to measure arterial flow at multiple times and locations. In most clinical MR studies, this method with balance SSFP or phase contrast variants, or direct compliance measurement using the cine gradient echo method is used to determine the changes in the cross-sectional area over the cardiac cycle. In conclusion, MR provides noninvasive means of determining arterial compliance with high potential for future advancements in the field of this technology [3].

LIMITATIONS

A patient's aorta cannot be explanted to measure compliance. Therefore a fluid flow model was used to validate the 1D method for measuring pulse wave velocity to estimate compliance.

CHAPTER 3 MATERIALS & METHODS

Since a patient's aorta cannot be explanted to measure compliance and MR provides a noninvasive means of determining arterial compliance, three (3) separate mini projects were initiated to validate the 1D method for measuring pulse wave velocity to estimate compliance. The three (3) mini projects are as follows and their importance described:

1. Measure and compare compliance values of tubes and MRI estimates using 1D method. Design model with segments including varying compliance values. *Importance: Need to validate if the compliance values of the tubing from the MRI estimates using 1D method is comparable to the compliance values of the tubing from mechanical testing methods.*
2. Check if 1D method can differentiate the different contributions to global compliance as a function of segment length. *Importance: Need flow phantom as a research test bench that will enhance the understanding of flow patterns with a specific geometry. Need flow phantom model to be sensitive enough to differentiate tubing with various compliances.*
3. Build analog electrical network model using estimated values from experimental measurements. *Importance: In vivo experimental studies used to study the effects of cardiovascular disease on arterial perfusion and peripheral pulse formation are both challenging and expensive to conduct and are limited to the easily accessible arteries. Consequently,*

the use of a computer model of the circulation offers an attractive alternative.

Work was done under the supervision of Dr. Gabriel Acevedo-Bolton as the primary researcher and Dr. David Saloner as the principal investigator at the University of California of San Francisco and Veteran Affairs Medical Center of San Francisco from July 2009 - December 2009.

ACRONYMS AND EQUATIONS

$D = (A_s-A_d) / A_d(P_s-P_d)$; where D is the arterial elasticity, A_s is the cross-sectional area under systolic conditions, A_d is the cross-sectional area under diastolic conditions, P_s is the systolic pressure, and P_d is the diastolic pressure

$D = 1/\rho V_{pw}^2$, Moens-Kortweg; where D is distensibility, ρ is density, and V_{pw} is pulse wave velocity

$E = d_i/h*\rho* V_{pw}^2$; where E is the modulus of elasticity, d_i is the inner diameter, h is the wall thickness, ρ is the density of the fluid, and V_{pw} is the pulse wave velocity of the fluid

$\varepsilon = \Delta L/L_0$; where ε is the mechanical strain, ΔL is the change in length, and L_0 is the initial length

σ=F/A; where σ is the mechanical stress, F is the force of the load on the latex tubing calculated by mass x gravitational acceleration, and A is the cross-sectional area of the latex tubing experiencing the load.

$E = \sigma / \varepsilon$; where E is Young's modulus of elasticity, σ is the mechanical stress, and ε is the mechanical strain.

$R = 8 \eta L / \pi r^4$; where R is resistance, η is viscosity, L is length, and r is radius

$L_{ind} = \rho L / \pi r^2$; where L_{ind} is inductance, ρ is density, L is length, and r is radius

$C_{cap} = 3\pi r^2 L / 2Eh$; where C is capacitance, r is radius, L is length, E is elastic modulus, and h is wall thickness

$C_{pwv} = \sqrt{E h_v / 2\rho r_{ID}}$; where E is elastic modulus, h_v is wall thickness, ρ is density, and r is inner radius

$E = 1/D(h/d_d)$; where E is elastic modulus, D is distensibility, h is wall thickness, and d_d is vessel inner diameter

$Q = \pi r^4 \Delta P / 8\eta L$; where Q is volumetric flow rate, r is radius, P is pressure, η is viscosity, and L is length

$\tau = 4\eta Q / \pi r^3$; where τ is shear stress, η is viscosity, Q is volumetric flow rate, and r is radius

$c = \sqrt{a/\rho\gamma} = \sqrt{Eh/2\rho a}$, where a is tube radius, ρ is density of blood, and γ = compliance of elastic tube

$\rho_{H2O} = 1\ g/cm^3$

$\rho_{blood} = 1.057 \pm 0.007\ g/cm^3$

η = viscosity = 10^{-3} Pa*s = 3.5 centipoise blood viscosity

FLOW PHANTOM

INTRODUCTION

When pathological modifications are produced, measurements of important parameters are observed to predict mass flow distribution. Therefore, circulation models offer a simplification of reality which helps to understand function. Many models have been developed for the aim of getting better insight and understanding of the relationship between physical phenomena within the human aorta, such as flow and pressure waveforms and the properties of the aorta itself, such as radius, wall thickness, distensibility and stiffness. The existence of various models is attributed mainly to the types of boundary conditions used, the nature of the vessel pressure-area relationship used, whether they are linear or nonlinear, and the method of solution [6]. Some models previously developed were intended to model the whole systemic circulation [33, 35, 38] and others focused on parts of the arterial system [40, 41]. The driving factor to build complex human arterial models is driven by a few goals. The major goal is being able to create a research test bench that will improve the understanding of flow patterns with a specific geometry, both one-dimensional and three-dimensional. Arterial elasticity is calculated directly by taking the change in vessel cross-sectional area and blood pressure and dividing by the cardiac cycle period,

$$D = (A_s - A_d) / A_d(P_s - P_d)$$

or indirectly by taking pulse wave velocity along the vessel,

$$D = 1/\rho V_{pw}^2.$$

MATERIALS

Flow Loop

A) Water tank
B) Gear pump
C) Garden Hose
D) Connectors
E) Rigid Tubing
F) LabView
G) Controller
H) Analog-to-Digital converter
I) Latex tubing

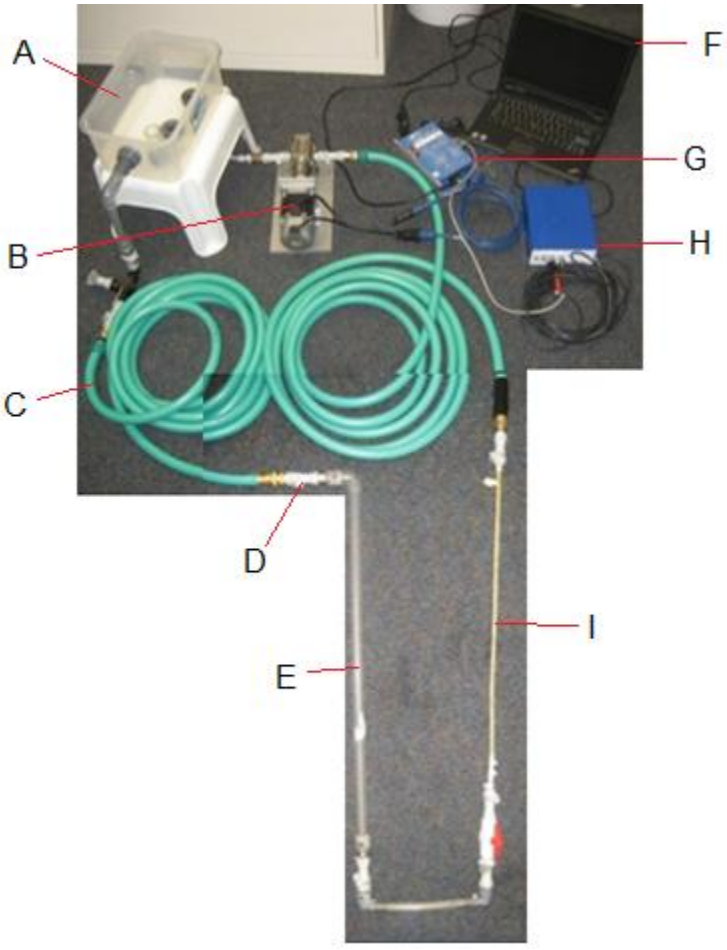

Figure 3.1. Flow phantom model and its parts

SETUP

Since the conditions under which the measurements were made may not be physiologically realistic, i.e. not distended to physiological pressure, the measurements taken from literature [6, 33, 59, 67] were used only to arrive at an estimate of the wall thickness of the aorta. Because material properties of latex were significantly different from that of the physiologic thoracic aorta, 1.2 MPa and 4 MPa, respectively, [6, 33, 59, 106, 107] various elastomers were researched for purchase and latex was the material of choice because Mc Master Carr manufactured the latex tubing with different wall thickness. With latex tubing coming in different wall thickness, the hope was to mimic a stiffer tube like that of the physiologic thoracic aorta.

Each tube in the phantom is represented by a single tube of constant diameter with circular cross section. Vessels with variable diameters could easily be incorporated into the phantom; however constant diameter greatly simplifies the phantom system as a whole.

Below is a table of the various latex tubing and its respective outer/inner diameters.

Table **3.1. Latex tubing and its respective dimensions**

Latex Tubing	Outer Diameter, inches	Inner Diameter, inches	Wall Thickness, inches
Latex 0	5/16”	1/4”	1/32”
Latex 1	5/8”	1/2”	1/16”
Latex 2	11/16”	1/2”	3/32”
Latex 3	3/4”	1/2”	1/8”
Latex 4	7/8”	1/2”	3/16”

FLOW PHANTOM CONSTRUCTION

General Approach

First, the model was divided into segments which could be represented as single units and the test specimen piece was attained through McMaster Carr. Determination of desired elasticity lied in the wall thickness shown in this equation:

$$E = d_i/h*\rho* V_{pw}^2,$$

where E is the modulus of elasticity, d_i is the inner diameter, h is the wall thickness, ρ is the density of the fluid, and V_{pw} is the pulse wave velocity of the fluid. For simplification purposes, length of the test specimen piece was straight during flow phantom testing.

Construction of the flow phantom system to model the cardiovascular system was performed by connecting rigid tubing in a continuous loop via hose connections. The idea was to construct a continuous loop with the water flowing from reservoir and back into it at the end of the loop. To complete the modeling of the cardiovascular system to acquire data on the compliance of a tube that represents the aorta or blood vessel, a

rigid tubing is removed to be replaced with an elastic latex tubing. The flow phantom is filled with water to act as the “blood” that flows through the system. The flow phantom is controlled by Labview software program and an analog-to-digital converter is used to convert the output signal from the computer to a control box which drives the gear pump. The gear pump is able to pump continuous flow or pulsatile flow depending on the controls of the user. In our case, continuous flow was used to remove all air bubbles to model physiologic blood vessels. During the experiment, pulsatile flow was used to pump a square wave waveform, which represents the left ventricle systolic behavior. The square wave waveform path starts from the gear pump pumping a specific pulsatile flow, next through some rigid tubing, then through some garden hose to bring the water from zone III (outside of the MRI room) to zone IV (inside of the MRI room), finally through the rest of the rigid tubing, lastly back into to reservoir. The square waveform travels consistently through the rigid tubing until it gets to the elastic tubing region where the square wave differentiates into a different waveform.

Flow Phantom assessment and characterization

Assessment of latex core diameters

The accuracy of the latex tubing geometric dimensions was assessed prior to testing by measuring the lumen diameters using vernier calipers. Diameters of all the latex tubing test specimens were found to agree well with the prescribed geometric dimensions.

Assessment of gear pump

The gear pump is able to pump continuously or pulsatilely depending on the controls of the user.

Assessment of Analog-to-Digital converter

Analog-to-digital converter is used to convert the signal output from the computer to the control box.

Assessment of Garden Hose

Garden hose is used as the rigid tubing to pump fluid from the outside of the MRI room (zone3) to the inside of the MRI room (zone4).

Assessment of flow characteristics of the model

To accurately test an imaging technique, the flow characteristics of the model must mimic those found in vivo. This includes the flow waveform measured at the inlet of the phantom, the flow velocity within the phantom, the flow division through the branches of the phantom, and the overall flow resistance of the phantom. Pulsatile square wave was produced at the inlet using a gear pump. Flow in the system was measured using GE scanner/Siemens scanner. That will be further discussed in the imaging section.

WHY IS IT SETUP THIS WAY

The flow phantom is setup to model the cardiovascular system, more specifically, the left ventricle and the aorta. It is setup in a continuous loop to resemble the cardiovascular system. It is setup with the testing specimen as elastic tubing to resemble a distensible aorta. The system receives a square wave from the gear pump to resemble the systolic behavior of the left ventricle. The reservoir is in place to pump a diastolic pump.

IMAGING

MATERIALS

- Flow phantom setup
- Cardiac Coil
- General Electric MRI Scanner with the Fourier Velocity Encoding
- Siemens MRI Scanner with the Phase Contrast Method

SETUP

The majority of the flow loop (garden hoses, connectors, rigid tubing, and elastic tubing) is placed in the scanner, in Zone IV, with the elastic tubing test specimen piece under the cardiac coil inside the core of the scanner. The remainder of the flow phantom is connected to the flow loop inside the MRI room (Zone III) via garden hoses.

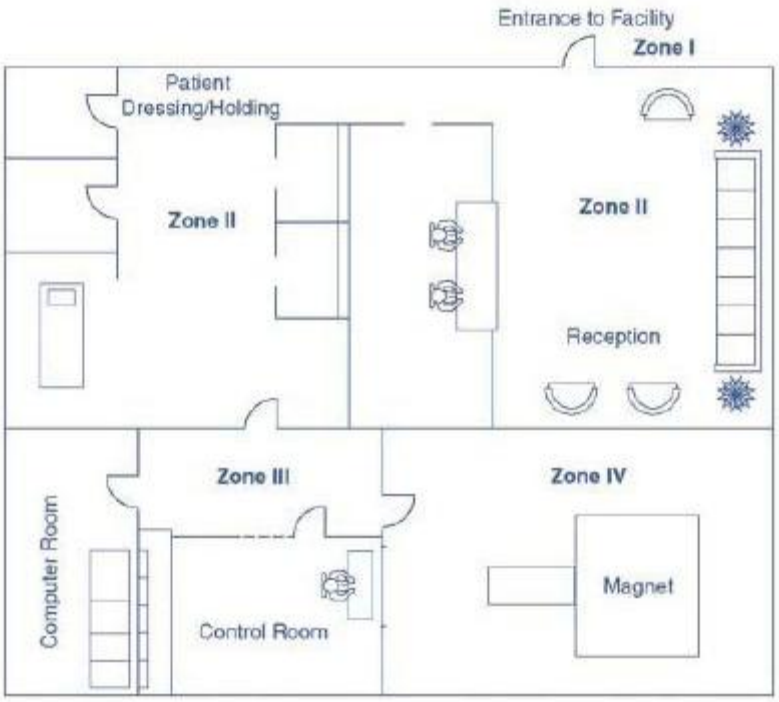

Sample floor plan illustrating various safety level zones in a typical magnetic resonance suite.
(Reprinted with permission from the American Journal of Roentgenology.)

Figure 3.2. Model Magnetic Resonance Facility Zone Configuration

HOW IT WORKS

Phase contrast method (Siemens) Algorithm

Phase contrast (PC) MRI was performed on the Siemens Avanto to measure the through-plane velocity at two offset slices. Since the offset distance is known, by measuring the time of travel of the velocity waveform of the water, we could calculate pulse wave velocity. Cross-sections of the latex tubing were included in the images and they were acquired as a function of time after a square wave in a plane orthogonal to the latex tubing. Determination of instantaneous flow was calculated using average flow

velocity and tubing cross-sectional area. Calculation of V_{pw} was determined from Eq. 9, where the travel time Δt was determined from the base of the flow wave in the proximal and distal tubing, and the distance between the two points Δs was determined by the length of the latex tubing. Utilization of retrospective gating to avoid distortions in the phase and omittance of non-velocity-encoded reference to reduce imaging time is a modification of the phase contrast method. [88]

ECG-gated phase contrast pulse sequence was built in [98] to improve spatial resolution and decrease scan times in which selection of one or more slices was substituted by the excitation of pencil-shaped regions [92, 93] (Figure 2.3) that move along the aorta. Additionally, a bipolar velocity-encoding pulse was utilized followed by a readout gradient, both applied longitudinally to the pencil beam. Next, the sequence was reiterated on the electrocardiographic (ECG) trigger below, with the inverse polarity of the bipolar pulse, and the difference in the signals from the two acquisitions was taken.

With a resolution time of 20-30 ms, repeating the sequence over several phases produces a scrolling display of position along the vessel vs. time, where intensity of the images is proportional to blood velocity. To decrease the effective resolution time, staggering the gating delay by 2-ms intervals and interleaving the results yields a total scan time averaging 32 heartbeats. Thus, the slope of the leading edge of the foot of the velocity trace is the pulsatile velocity.

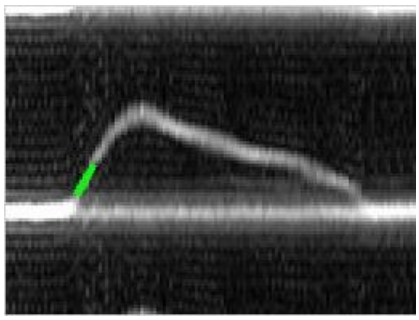

Figure 3.3. Blood flow vs. time in the latex tubing. Slope of the leading edge of the foot of the velocity trace is the pulsatile velocity.

Fourier velocity encoding (General Electric) Algorithm

Direct measurement of pulse wave velocity was performed by implementing Fourier-Velocity Encoding on the General Electric MRI. The capability to measure the distribution of velocities within a voxel [94, 95], which enhances the visualization of the velocity waveform as it propagates down the tubing is an advantage of Fourier-velocity encoding over phase contrast method. The sequence was repeated at multiple phases of the pump cycle resulted in a video of water velocities where the flow wave can be seen as propagating from slice-to-slice. A various ECG-gated method combined the pencil excitation with the Fourier velocity encoding method to create videos of water velocity distributions which is similar to the results from a Doppler M-mode pulse sequence [97]. Pulse sequence utilized was similar to an earlier study [98], except the bipolar velocity encoding gradient was stepped to a new value on each ECG trigger, typically through a total of 16 steps (Figure.2.3, bottom). Then the collected signals were “Fourier transformed to produce a velocity spectrum on the horizontal axis as a function of position along the pencil on the vertical axis" (Figure 3.4).

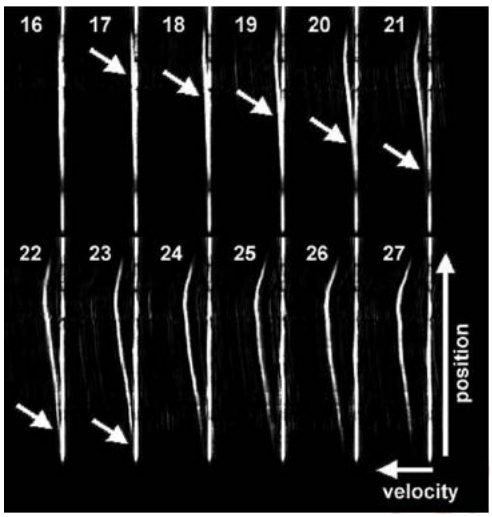

Figure 3.4. Velocity as a function of position along pencil. Frames 16–27 from Fourier velocity-encoded M-mode data set from descending aorta of normal volunteer, showing propagation of foot of flow wave (arrows) down the aorta. Field of view (vertical axis) was 240 cm zoomed to 190 cm; time per frame was 3.6 ms; wave velocity was 550 cm/s.

WHY IS IT SETUP THIS WAY

Water flow waveforms were measured in the latex tubing at multiple imaging sections using phase contrast velocity imaging and Fourier-velocity encoding imaging. The pulses are set up as a basic step function with a period of 1 second. This was the baseline period for both the GE and Siemens scanner. The inputs into the pump is not as important as the relation between the pulses and the velocity waveform in the tubing, which looks nothing like the waveform input to the pump due to compliance, reflections, etc. In this study, a near step function was sent to the pump, but the resultant flow in tubes was a bi-peaked smoothed out curve. The basic pulse was chosen because it

was simple to implement and resulted in a pseudo-physiological looking waveform in the tubing.

THE PARAMETERS

GENERAL ELECTRIC

The MR images of phantom filled with water were acquired using a cardiac coil in a 1.5T whole magnet GE scanner. A Fourier-velocity encoding technique with the following parameters was used:

- VENC 60, 65, 75 cm/s
- Pencil beam diameter 1cm, 1.5cm, 2cm
- Gradient Echo Pulse Sequence
- Flip angle 45°
- Bandwidth 15.63
- Field of View 32cm
- Slice thickness 7mm
- Spacing 1.5 cm
- Frequency 256 Hz
- Phase 64
- Nex 1
- Cardiac gating
- Respiratory trigger
- Waveform multiplier 2.5x - 4.0x

SIEMENS

The MR images of phantom filled with water were acquired using a cardiac coil in a 1.5T whole magnet Siemens scanner. A phase contrast technique with the following parameters of interest:

- Amplitude: Main_pulse, 2x_pulse, 4x_pulse, 8x_pulse, 1/2x_pulse

- Pulse length: Main_pulse, 2x_length, 4x_pulse, 1/2x_length
- VENC 30, 50 cm/s
- Repetition Time (TR) 17.30 ms
- Echo Time 5.35 ms
- Slice thickness 10 mm
- Bandwidth 343
- Field of View 180 mm (phase = 50%)
- Gadolinium was added 1:100 by volume

WHY THESE PARAMETERS?

General Electric

- VENC (velocity encoding) is a specialized technique for encoding flow velocities. It can used to measure several hemodynamic properties of blood flow. The maximum velocity within a vessel can be easily determined by finding the pixel within the voxel which has the greatest displacement in the velocity dimension. Since the intensity of each pixel in a velocity image is proportional to the number of spins moving at a given velocity and in a given location, the mean velocity and the width of the velocity distribution can be determined.
- Pencil Beam Diameter is area of interest where the 1D MRI images are collected. A smaller diameter will require less time and collect less data. A larger diameter will require more time and collect more data. An analogy would be that the

smaller diameter would look more like a sharper bell curve where as a larger diameter will look more like a flatter bell curve.

- Gradient Echo Pulse Sequence was used to get the shortest possible Repetition Time and Scan Time. It is first used in reverse to enforce a transverse dephasement of spinning protons. Right after, it is used as a readout gradient to realign the dephased protons and therefore acquire signal.
- Flip Angle is the angle to which the magnetization is rotated or tipped relative to the main magnetic field direction via the application of radio-frequency (RF) pulse. The Flip Angle is used to define the angle of excitation for the Gradient Echo Pulse Sequence. With the use of Flip Angles, Repetition Time (TR) scan time can thus be reduced without producing saturation. For example, for saturation, flip angle should be large and TR should be short so that full recovery cannot occur. To prevent saturation, flip angle should be small and the TR long enough to permit full recovery.
- Bandwidth refers to the preselected band or range of frequencies which can govern both slice select and signal sampling.
- Field of View is the size of the two dimensional spatial encoding area of the image.
- Slice thickness is the thickness of the imaging slice.
- Spacing is the distance between each imaging slice.
- Frequency is the number of cycles or repetitions of any periodic wave or process per unit time.

- Phase is the angular relationship describing the degree of synchronism between two sinusoidal waveforms of the same frequency.
- NEX (Number of excitations) is referred to an indicator of how many times each line of k-space data is acquired during the scan.
- Cardiac gating is timing the acquisition of MR data to phantom “cardiac” motion in order to minimize motion artifacts.
- Respiratory trigger refers to the type of phantom “respiratory” motion. The images are acquired during the “expiration” phase.
- Waveform multiplier is the magnitude of change in the amplitude of the input waveform.

Siemens

- The pulse amplitude, length, and frequency are not important, but rather how the pulses related to one another.
- VENC (velocity encoding) is a specialized technique for encoding flow velocities. It can used to measure several hemodynamic properties of blood flow. The maximum velocity within a vessel can be easily determined by finding the pixel within the voxel which has the greatest displacement in the velocity dimension. Since the intensity of each pixel in a velocity image is proportional to the number of spins moving at a given velocity and in a given location, the mean velocity and the width of the velocity distribution can be determined.
- Repetition Time is the time that exists between successive pulse sequences applied to the same slice.
- Echo Time is the time between the application of the 90° pulse and the peak of the echo signal.
- Slice thickness is the thickness of the imaging slice.
- Bandwidth refers to the preselected band or range of frequencies which can govern both slice select and signal sampling.
- Field of View is the size of the two dimensional spatial encoding area of the image.
- Gadolinium is used to boost signal.

POST ANALYSIS

HOW POST ANALYSIS WORKS

Fourier velocity encoding method

The MR FVE M-mode pulse sequence is helpful for quantifying both blood velocity and pulse-wave velocity in a designated artery. Consequently, the second quantity can be used to determine arterial distensibility noninvasively. The algorithm generates a time series of blood velocity traces over the cardiac cycle, which can be played together as a video. In each trace, the horizontal is blood velocity and the vertical axis shows position along the artery. In the collection of data throughout the cardiac cycle, a waveform can be seen rising from the baseline zero-velocity line, growing to a peak value of blood velocity, and then returning back to zero. In a closer look, the foot of the velocity waveform and be seen to move vertically in successive frames, reflecting the propagation of the velocity wave along the artery, from proximal to distal portions. Measurement of the relative position of the various waveforms allows the quantification of pulse-wave velocity. The analysis tools accomplishes this by first converting the data to a velocity-time presentation; next, finding the location in time of the foot of each waveform; then, plotting time of the foot versus position; and finally, generating a best fit to the data.

MECHANICAL TESTING

INTRODUCTION

The following study was to determine the stiffness across a small range of strain and linear properties of latex tubing with ranging thicknesses, therefore distensibility or

Young's modulus. Latex tubing was subjected to displacement-controlled stretch testing. The understanding of material properties such as stiffness and wall stress is important in the study of blood vessel biomechanics. Determination of material properties of latex tubing was the objective of this study. Uniaxial tensile testing was performed below, within, and beyond physiological ranges of strain to gain an understanding of this elastic material under specific physiologic conditions.

OBJECTIVE

1) Measure compliance values of elastic tubing using tensile testing;

2) Determine pulse wave velocity to estimate compliance values using the MRI 1D method;

3) Compare compliance values.

MATERIALS

McMaster Carr provided the latex tubing for the uniaxial tensile testing. Because of the similar anatomy and biomechanics to human aorta, latex tubing was the selected material. Latex tubing thickness was measured with calibrated calipers. Latex tubing is an isotropic plastic, thus orientation was not vital for determining mechanical properties.

SETUP

Uniaxial stretch testing

Cut of tubing and Loading Orientation of Latex Sample

Latex tubing was cut on-end to produce a 1 in. long piece of tubing which was cut length-wise. The tubing was flattened out and additional cuts were made to produce a 1 in. x 1 in. square test sample. Because the latex is made in such a way that the material curls inward circumferentially when unloaded and flattens out when loaded, latex tubing must be loaded longitudinally to reduce preload or else this puts a preload on the load cells before initial stretching. This was taken into account; however, this is not physiologically consistent. As a result, the stress-strain plot may appear stiffer or less stiff due to the preload causing early deformation making material enter into plastic deformation when testing starts.

How it works and why it is setup this way

Uniaxial tensile testing is an industry standard. As expected, an in-house uniaxial stretcher was used for the determination of material properties. Two 5-0 silk sutures were used to anchor each edge of the specimen by hooking fishhooks which were attached to two linear arms of the uniaxial stretcher. A five black ceramic marker 3mm x 3mm grid was placed at the center of the specimen. The displacement of the markers was the essential, not the precision of the created grid. Load cells (Model 31/3672-02, Honeywell Sensotec Inc., Columbus, OH, 1000 gm; ±0.1%), placed on two orthogonal arms were tarred (zeroed) and checked post-sample set up to ensure a zero force

measurement corresponding to each specimen at rest in the uniaxial directions. Throughout tensile testing, data from load cells was connected to amplifier and utilized to find out the force on latex tubing under extension deformation. Utilizing a real-time non-contacting CCD camera (30fps, Model TM9701, Pulnix Inc., Sunnyvale, CA; 0.1pixels/mm), displacement of the five markers on latex tubing surface was collected. Digitization using MATLAB software was carried out on .TIFF files by tracking marker displacement in the two planar alignments relative to the surrounding tissue and their displacement. Calculations of the stress and strain are plotted in the principal direction.

Data Collection and Analysis

To study material properties at systemic pressures, samples of latex tubing over a range of strain were stretched. Stretch tests were performed to 1%, 2%, 5% peak strain. A thin specimen was assumed. Thus, stress experienced by the sample was zero. Assuming sample deformation at a constant volume at this relatively low strain is noted as the incompressibility assumption.

Mechanical tensile testing

Latex tubing obtained from McMaster Carr was used for validation of the previous uniaxial stretch testing. A cross-sectional area, the wall thickness of the latex tubing was measured with calibrated calipers. Proximal end of latex tubing was fixed using C-clamp. The C-clamp was then fixed in place by another C-clamp kept in place by clamping on a horizontal flat surface. Preloaded length of the latex tubing was

measured to determine initial length. Load was added to the distal end of the latex tubing by clamping a C-clamp and hooking on additional C-clamps as weights. Post loaded length of the latex tubing was then measured. Equations of interest include the strain equation:

$$\varepsilon = \Delta L/L_0,$$

where ε is the mechanical strain, ΔL is the change in length, and L_0 is the initial length and,

$$\sigma = F/A$$

where σ is the mechanical stress, F is the force of the load on the latex tubing calculated by mass x gravitational acceleration, and A is the cross-sectional area of the latex tubing experiencing the load.

This method of mechanical tensile testing was repeated for five different latex tubing with varying wall thicknesses, consequently, distensibility. Distensibility, or Young's modulus of elasticity, was determined using Microsoft Office Excel. Equation of interest is

$$E = \sigma/ \varepsilon,$$

where E is Young's modulus of elasticity, σ is the mechanical stress, and ε is the mechanical strain. An incompressibility assumption was made where the samples deform at a constant volume.

ELECTRICAL ANALOG NETWORK MODEL

INTRODUCTION

Blood flow pulses and arterial pressure which result from the interaction of the arterial system and the heart have been a valuable resource in the assessment of cardiovascular disorder.

Industrial Significance

Computer modeling of the arterial circulation presents a desirable option [32-40]. Models are utilized to assist the simplification and understanding of function in reality.

The integrated, one-dimensional continuity and momentum governing equations make up the foundation of the computer modeling. Differences between models are attributed to: (a) boundary conditions, (b) the nature of the vessel pressure-area relationship, (c) whether they are linear or nonlinear, and (d) and the method of solution [6]. Some models aim to model the entire systemic circulation [33, 35, 38], and others concentrated on parts of the arterial system [40, 41]. To validate the competency of the fluid flow model to accurately simulate arterial flow, measurements are compared to experimental findings.

Electrical Network modeling

To attain an improved intuition and knowledge of human aortic physical phenomena relationships such as pressure and pulsatile flow waveform transmission, and the properties of the aorta itself, such as radius, wall thickness, distensibility, and stiffness,

electronic analog models need to be developed. The class of model of interest in this section is physical models utilizing hydrodynamic or electrical analogs [33]. Models are founded on electromechanical analogs, transmission system of elastic tubing and an electrical transmission line, able to predict blood pressure and flow waveforms, given initial conditions of mechanical properties and parameters of the dimensions of the arterial system [67]. The model developed has a limited clinical application because it does not include autoregulation and does not respond to dynamic situations [54]. Frank [71] later quantitatively devised and popularized the two-element Windkessel model which consisted of a resistance and capacitance element. According to Poiseuille's law, the resistance is inversely proportional to blood vessel radius to the fourth power. Driven by total resistance and total capacitance, the original Windkessel model's aorta [68] behaves as an expandable chamber in which diastolic pressure decays exponentially with a time constant; fine tuning of the model included the inductance to resemble blood inertia [69, 70]. Hales suggested that the differences in pressure waveforms had a correlation with the distensibility of large arteries, more specifically, the aorta [77]. Total resistance to flow in the overall arterial system is mostly largely found in the resistance of the collection of small arteries and the arterioles. The summation of the total peripheral resistance includes the resistance of the total systemic vascular bed and is calculated by the addition of every individual resistance in the microcirculation. The peripheral resistance, R, is determined as:

$$R = (P_{ao,\,mean} - P_{ven,\,mean})/CO \approx P_{ao,\,mean}/CO \qquad (5)$$

with $P_{ao,\,mean}$ and $P_{ven,\,mean}$ mean aortic and venous pressure and CO cardiac output. [77].

Total capacitance is mostly determined by the distensibility of the large or intermediate arteries. The summation of the entire arterial compliance is determined by the sum of all the compliances of the arterial system. The entire arterial compliance, C, is the ratio of the change in volume, ΔV, and the resultant change in pressure ΔP:

$$C = \Delta V / \Delta P \quad (6)$$

The two-element Windkessel model expects that in diastole, aortic valve closed at end-systole, pressure waveforms decay exponentially specified a characteristic decay time RC. In a previous study, Frank's objective was to attain cardiac output. An independent initial condition estimate of total arterial capacitance would calculate the total peripheral resistance with the characteristic decay time RC when derived from the aortic pressure at end-systole (in diastole). Thus, the cardiac output is the average velocity of blood flow which is the change in aortic pressure divided by the regional peripheral resistance. Consequently, Frank, is able to calculate total arterial compliance from pulsatile velocity waveforms in the aorta [77].

OBJECTIVE

Build analog electrical network model using estimated values from experimental measurements.

MATERIALS

Simulink was used in integration with Matlab to build the analog electrical network model. Conversion of experimental values from phantom model to electrical elements was attempted. Values were unreliable due to material and component uncertainties.

SETUP

Equations of interest include:

$$R = 8\mu/\pi r^4 \quad (11)$$

$$L = \rho/\pi r^2 \quad (12)$$

$$C = 3\pi r^2/2Eh \quad (13)$$

where R = resistance per unit length; L = inductance per unit length; C = capacitance per unit length; μ = blood viscosity; r = radius; ρ = blood density; E = Young's modulus; and h = arterial wall thickness. [67]

Underdamped: $R^2-4L/C < 0$

$$R_u = 5.0 \times 10^{-3}$$

$$L_u = .7 \times 10^{-3}$$

$$C_u = 1 \times 10^{1}$$

Model of interest includes voltage source vs. current source to represent the cardiac and series circuit vs. parallel circuit to represent the aorta.

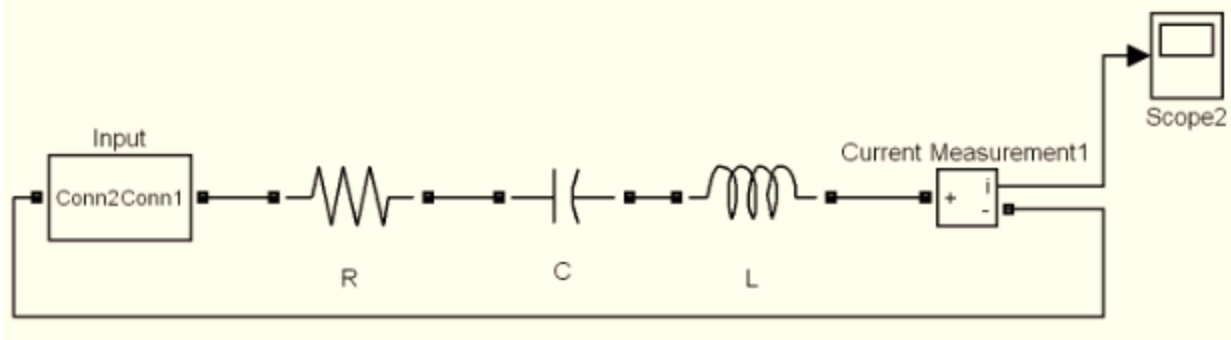

Figure 3.5. Voltage source in series circuit electrical analog network model.

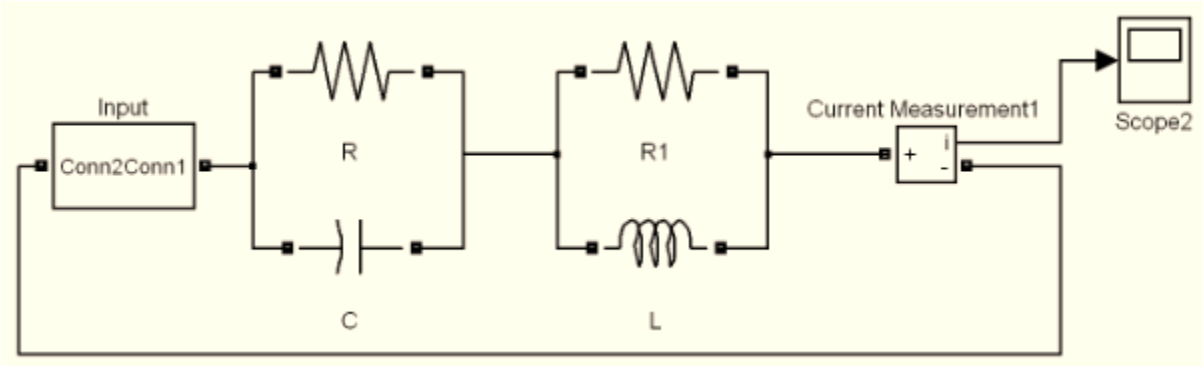

Figure 3.6. Voltage source in parallel circuit electrical analog network model.

HOW IT WORKS

Explain how voltage = pressure, current = flow, resistance = friction; R = friction in system, L= blood inertia, C = compliance or distensibility

The governing equations [5, 33, 77] for blood flow can be linearized in terms of change in pressure *p* and flow rate *q* in which flow properties are analogous to a segmental electric circuit as:

Voltage V ≡ p (pressure)

Current	$I \equiv q$	(flow rate)
Inductance	$L \equiv \rho/A$	(blood density/lumen area)
Resistance	$R \equiv \mu\rho l/A$	(absolute viscosity*blood density*lumen length/lumen area)
Capacitance	$C \equiv \Delta V/\Delta P$	(change in volume/change in pressure)

WHY IS IT SETUP THIS WAY?

Parallel paths in the circuit introduce distinct (i.e. different) currents flowing through each branch in the parallel paths. Since the current is analogous to flow velocity, one length of tubing cannot simultaneously have two different flow velocities unless there are separate and parallel tubes. The series representation models the characteristics of the tubing, both the resistive non-compliant behavior as well as the capacitive compliant behavior. We have also included the inductor to model the flow inertia however, in our model, there is only one flow velocity at any given instant of time that is possible since the elements are series connected.

CHAPTER 4 RESULTS

IMAGING USING FLOW PHANTOM

The flow phantom was setup to model the left ventricle and the aorta. The continuous loop resembles the cardiovascular system. The testing specimen is elastic tubing that resembles the distensible aorta. Pulsatile flow was produced at the inlet using a gear pump representing the left ventricle systolic behavior which travels consistently through the rigid tubing until it gets to the elastic tubing region where the input square wave (Figure 4.1) differentiates into different waveforms.

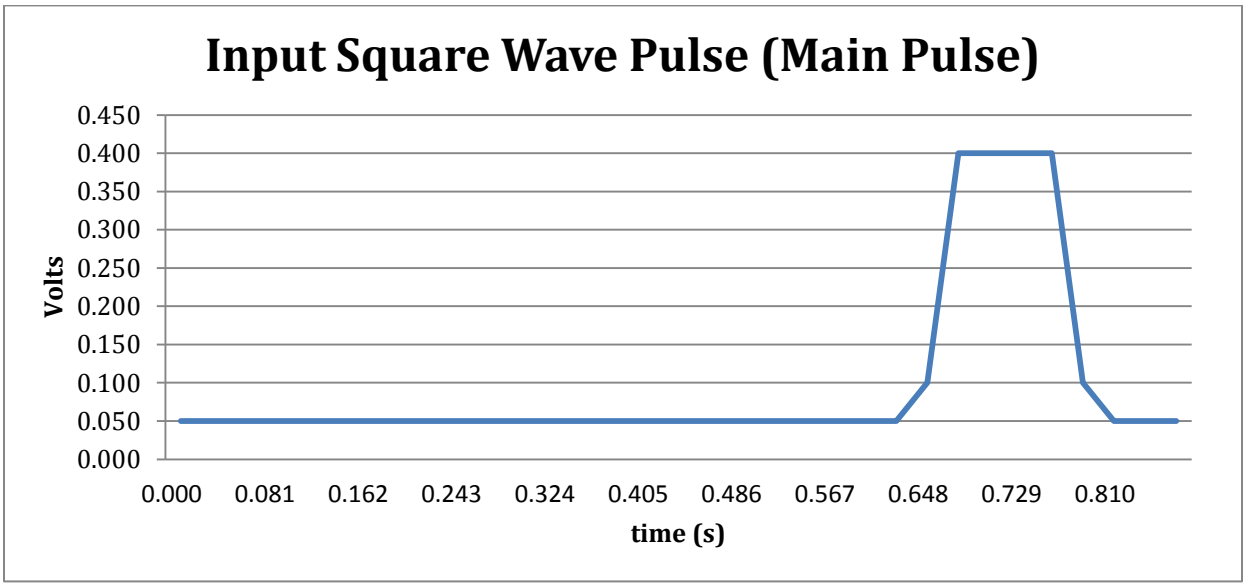

Figure 4.1. Input waveform through flow phantom. Input waveform (Main Pulse) through the flow phantom for imaging via phase contrast method and Fourier velocity encoding method.

PHASE CONTRAST METHOD

Phase contrast (PC) MRI was performed on the Siemens Avanto to measure the through-plane velocity at two offset slices. Since the offset distance is known, by measuring the time of travel of the velocity waveform of the water, we could calculate pulse wave velocity. The pulsatile flow produced at the inlet using the gear pump differentiates into the different waveforms (Figure 4.2) below. Various latex tubing (Latex 1, 2, 3, and 4) was used to replace a rigid tubing. In Figure 4.2, the mean velocity decreases as a function of wall thickness increase.

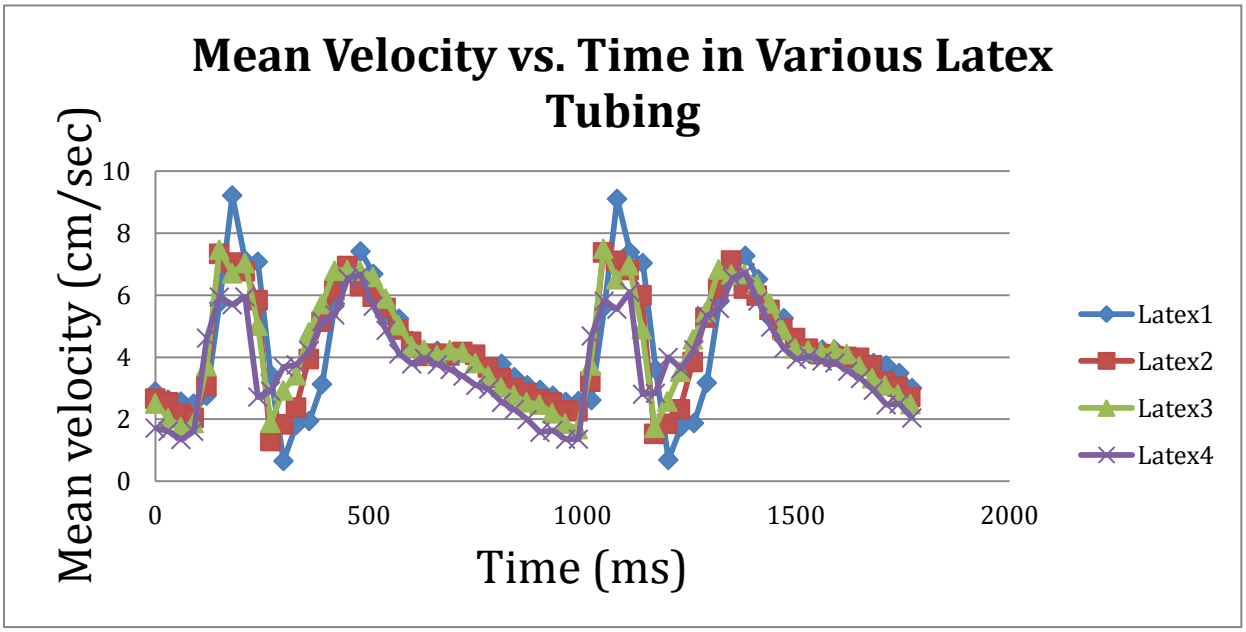

Figure 4.2. Mean velocity output profile in various latex tubing using Phase Contrast Method. The mean velocity output profile in various latex tubing using the phase-contrast method in the Siemens MRI with the input waveform, Main Pulse. Mean velocity decreases as a function of wall thickness increase. Experiment performed September 24, 2009.

With Latex 1 in place, various square wave pulses were inputted into the flow phantom using the phase-contrast method in the Siemens MRI. The main pulse or 1x duty refers to the original length of the input square wave pulse. 2x duty of main pulse refers to 2x the length of the input square wave pulse. 3x duty of main pulse refers to 3x the length of the input square wave pulse. 4x duty of main pulse refers to 4x the length of the input square wave pulse. The output waveform is plotted relative to one another to observe the effects of varying the input square waveform. In Figure 4.3, mean velocity increases as a function of length of input square waveform increase.

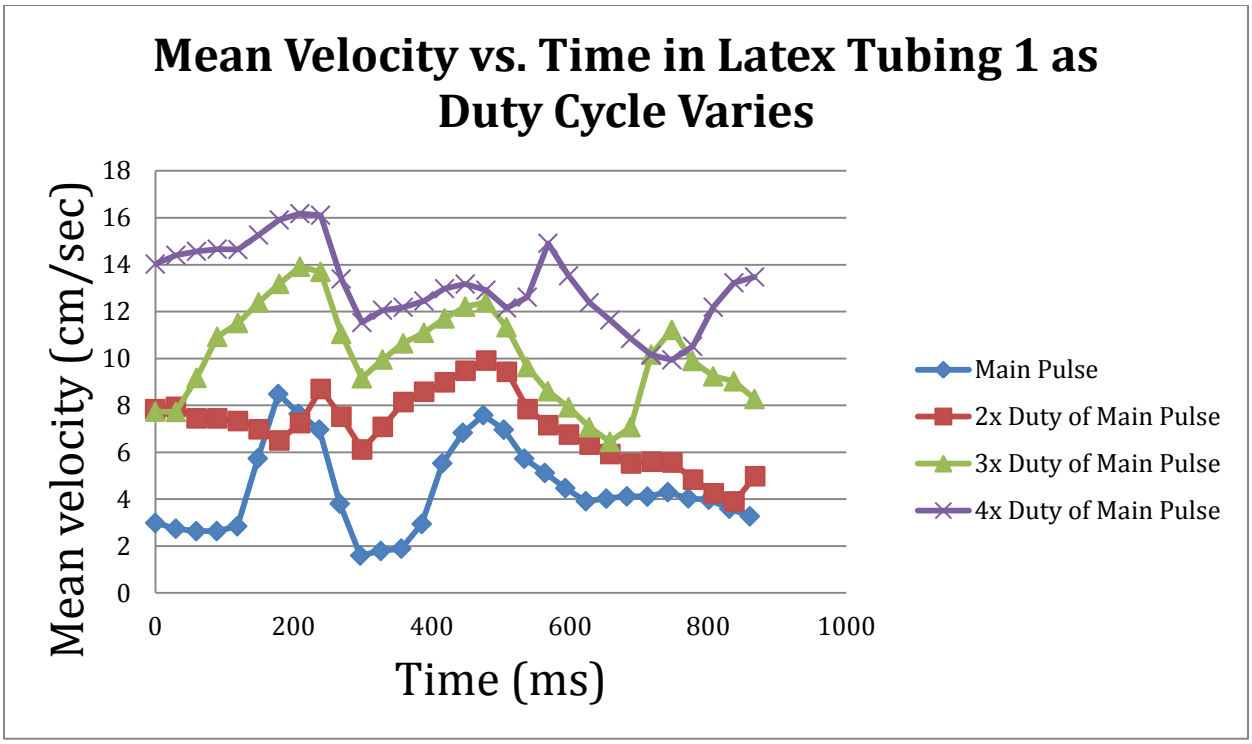

Figure 4.3. Mean velocity output profile through latex tubing 1 using phase contrast method with various duty cycles. The mean velocity output profile through latex tubing 1 using the phase-contrast method in the Siemens MRI with various duty cycles of the Main Pulse. The main pulse or 1x duty refers to the original length of the input square wave pulse. 2x duty of main pulse refers to 2x the length of the input square wave pulse. 3x duty of main pulse refers to 3x the length of the input square wave pulse. 4x duty of main pulse refers to 4x the length of the input square wave pulse. The output waveform is plotted relative to one another to observe the effects of varying the input square waveform. Mean velocity increases as a function of length of input square waveform increase. Experiment performed October 5, 2009.

With Latex 1 in place, various amplitudes of the square wave pulse were inputted into the flow phantom using the phase-contrast method in the Siemens MRI. The main

pulse refers to the original amplitude of the input square wave. 1/2 amplitude refers to 1/2 the amplitude of the original amplitude of the input square wave. 2x amplitude refers to 2x the amplitude of the original amplitude of the input square wave. The output waveform is plotted relative to one another to observe the effects of varying the input square waveform. In Figure 4.4, mean velocity increases as a function of amplitude of input square waveform increase.

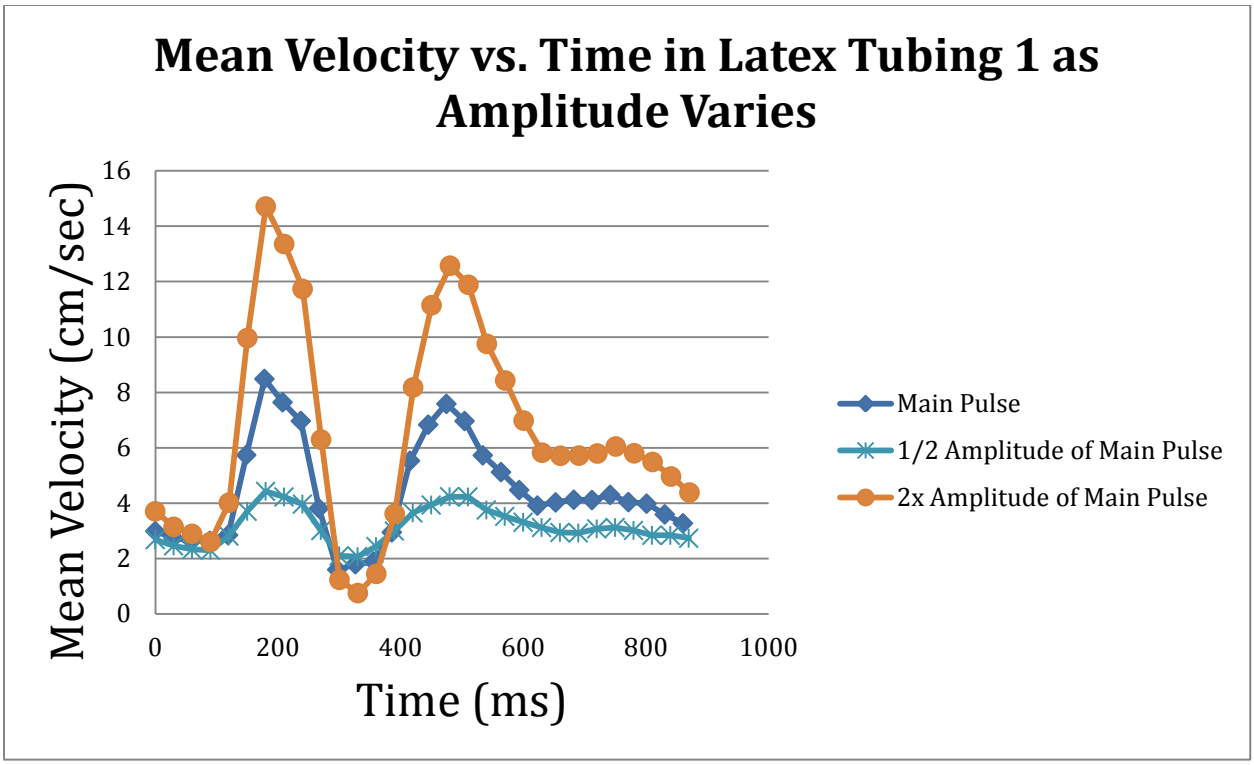

Figure 4.4. Mean velocity output profile through latex tubing 1 using phase contrast method with various amplitudes. The mean velocity output profile through latex tubing 1 using the phase-contrast method in the Siemens MRI with various amplitude of the Main Pulse. Main pulse refers to the original amplitude of the input square wave. 1/2 amplitude refers to 1/2 the amplitude of the original amplitude of the input square wave. 2x amplitude refers to 2x the amplitude of the original amplitude of the input square wave. The output waveform is plotted relative to each input waveform. Mean velocity increases as a function of amplitude of input square waveform increase. Experiment performed October 5, 2009.

With Latex 1 in place, various square wave pulses were inputted into the flow phantom using the phase-contrast method in the Siemens MRI. The main pulse or 1x duty refers

to the original length of the input square wave pulse. 2x duty of main pulse refers to 2x the length of the input square wave pulse. 3x duty of main pulse refers to 3x the length of the input square wave pulse. 4x duty of main pulse refers to 4x the length of the input square wave pulse. The output waveform is plotted relative to one another to observe the effects of varying the input square waveform. In Figure 4.5, mean velocity increases as a function of length of input square waveform increase.

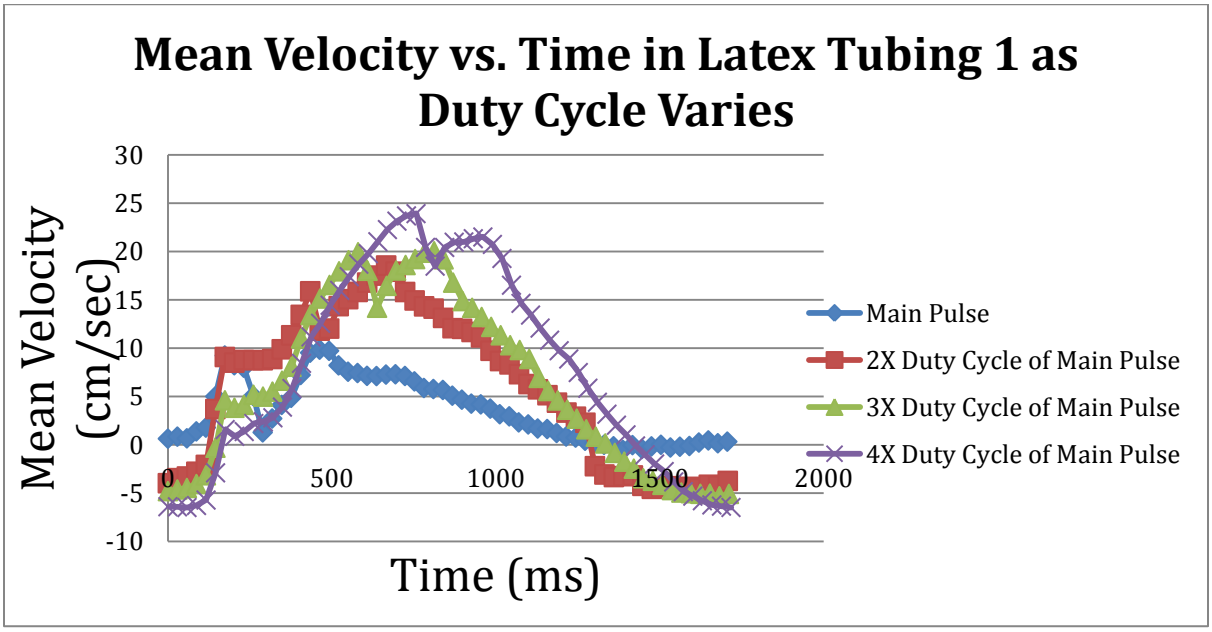

Figure 4.5. Mean velocity output profile through latex tubing 1 using phase contrast method with various duty cycles. The mean velocity output profile through latex tubing 1 using the phase-contrast method in the Siemens MRI with various duty cycles of the Main Pulse. Main pulse, 1x duty, refers to the original length of the input square wave. 2x duty of main pulse refers to 2x the length of the input square wave, and so on. The output waveform is plotted relative to each input waveform. Mean velocity increases as a function of length of input square waveform increase. Experiment performed October 8, 2009.

With Latex 1 in place, various amplitudes of the square wave pulse were inputted into the flow phantom using the phase-contrast method in the Siemens MRI. The main pulse refers to the original amplitude of the input square wave. 2x amplitude refers to 2x the amplitude of the original amplitude of the input square wave. The output waveform is plotted relative to one another to observe the effects of varying the input square waveform. In Figure 4.6, mean velocity increases as a function of amplitude of input square waveform increase.

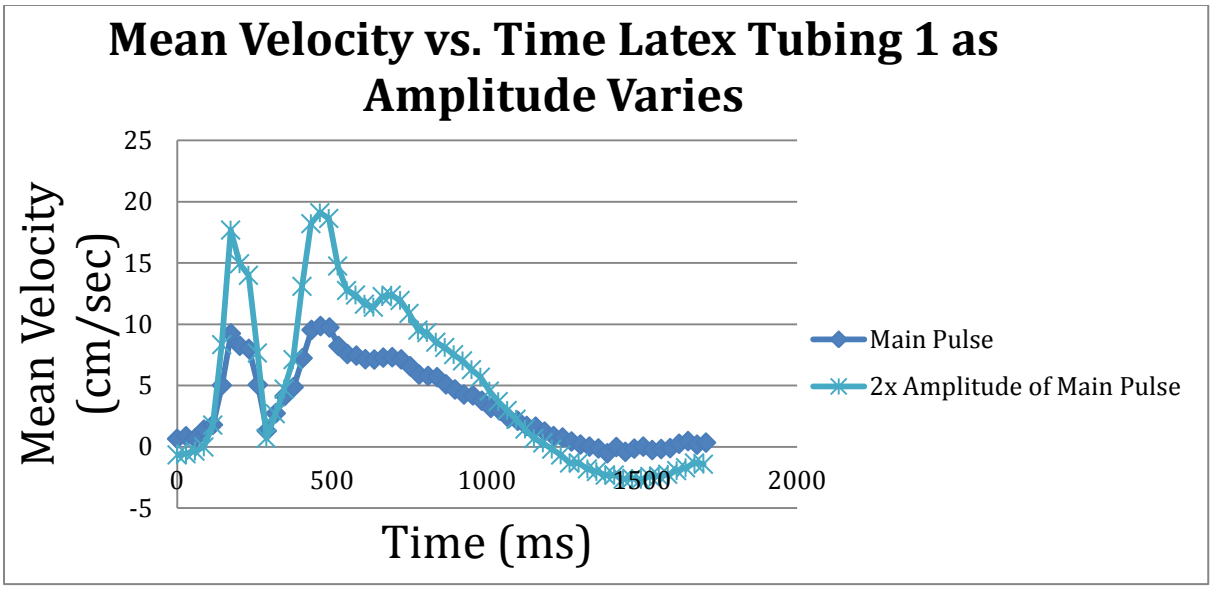

Figure 4.6. Mean velocity output profile through latex tubing 1 using phase contrast method with various amplitudes. The mean velocity output profile through latex tubing 1 using the phase-contrast method in the Siemens MRI with various amplitude of the Main Pulse. Main pulse refers to the original amplitude of the input square wave. 2x amplitude refers to 2x the amplitude of the original amplitude of the input square wave. The output waveform is plotted relative to each input waveform. Mean velocity increases as a function of amplitude of input square waveform increase. Experiment performed October 8, 2009.

With Latex 4 in place, various square wave pulses were inputted into the flow phantom using the phase-contrast method in the Siemens MRI. The main pulse or 1x duty refers to the original length of the input square wave pulse. 2x duty of main pulse refers to 2x the length of the input square wave pulse. 3x duty of main pulse refers to 3x the length of the input square wave pulse. 4x duty of main pulse refers to 4x the length of the

input square wave pulse. The output waveform is plotted relative to one another to observe the effects of varying the input square waveform. In Figure 4.7, mean velocity increases as a function of length of input square waveform increase.

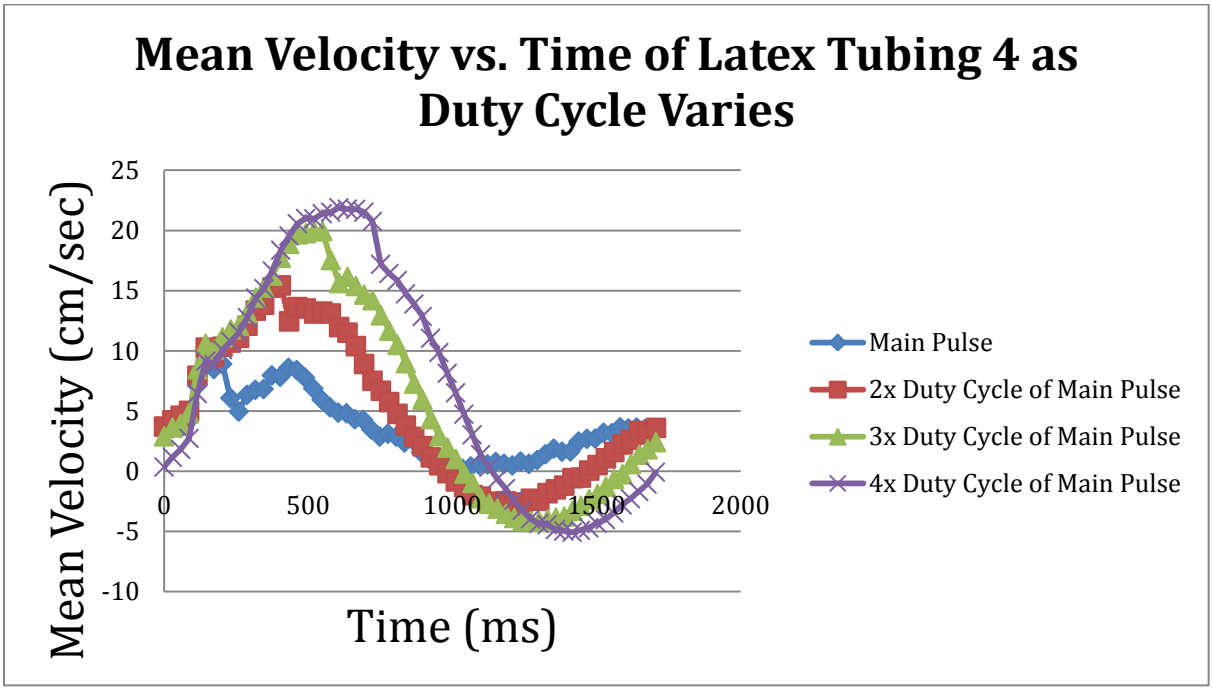

Figure 4.7. Mean velocity output profile through latex tubing 4 using phase contrast method with various duty cycles. The mean velocity output profile through latex tubing 4 using the phase-contrast method in the Siemens MRI with various duty cycles of the Main Pulse. Main pulse, 1x duty, refers to the original length of the input square wave. 2x duty of main pulse refers to 2x the length of the input square wave, and so on. The output waveform is plotted relative to each input waveform. Experiment performed October 8, 2009.

With Latex 4 in place, various amplitudes of the square wave pulse were inputted into the flow phantom using the phase-contrast method in the Siemens MRI. The main pulse refers to the original amplitude of the input square wave. 2x amplitude refers to 2x the amplitude of the original amplitude of the input square wave. The output waveform is plotted relative to one another to observe the effects of varying the input square waveform. In Figure 4.8, mean velocity increases as a function of amplitude of input square waveform increase.

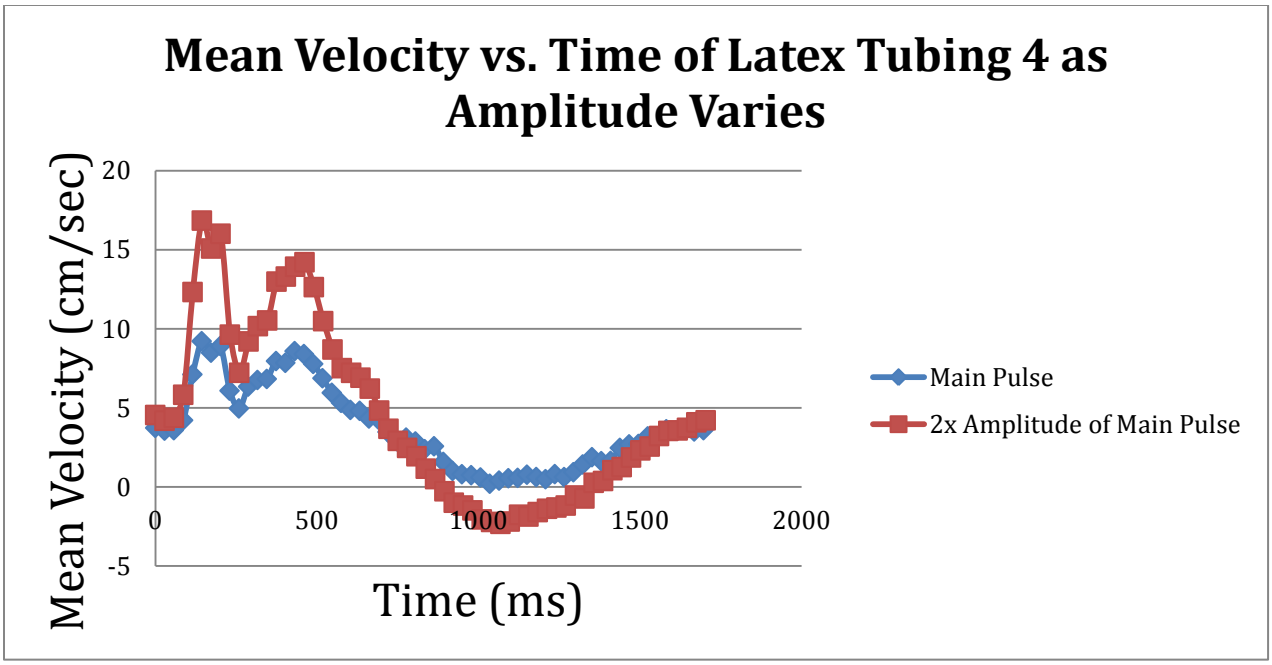

Figure 4.8. Mean velocity output profile through latex tubing 4 using phase contrast method with various amplitudes. The mean velocity output profile through latex tubing 4 using the phase-contrast method in the Siemens MRI with various amplitude of the Main Pulse. Main pulse refers to the original amplitude of the input square wave. 2x amplitude refers to 2x the amplitude of the original amplitude of the input square wave. The output waveform is plotted relative to each input waveform. Experiment performed October 8, 2009.

FOURIER VELOCITY ENCODING

Fourier-Velocity Encoding was implemented on the General Electric MRI to directly measure pulse wave velocity. An advantage of the Fourier-velocity encoding method of the phase contrast method is that it has the capability to measure the distribution of velocities within a voxel [94, 95], which enhances the visualization of the velocity

waveform as it propagates down the tubing. The sequence was repeated at multiple phases of the pump cycle resulted in a video of water velocities where the flow wave can be seen as propagating from slice-to-slice. Water flow waveforms were measured in the latex tubing at multiple imaging sections using Fourier-velocity encoding imaging.

Table 4.1. Pulse wave velocity in various latex tubing using Fourier-velocity encoding method. Pulse wave velocity increases from latex 1 to latex 4. Experiment performed November 10, 2009.

Tubing	**Inner diameter**	**Outer diameter**	**Wall thickness**	**Pulse wave velocity**	**Distensibility**
latex 1	1/2"	5/8"	1/16"	5.6 m/s	3.2E-05 Pa^-1
latex 2	1/2"	11/16"	3/32"	7.1 m/s	2.0E-05 Pa^-1
latex 3	1/2"	3/4"	1/8"	11.8 m/s	7.2E-06 Pa^-1
latex 4	1/2"	7/8"	3/16"	11.9 m/s	7.1E-06 Pa^-1

MECHANICAL TESTING

Mechanical testing was used to determine the stiffness across a small range of strain and a small range of strain and linear properties of latex tubing with ranging thicknesses, therefore distensibility or Young's modulus. The understanding of stiffness and wall stress is important in the study of blood vessel biomechanics.

UNAXIAL STRETCH TESTING

Uniaxial tensile testing is an industry standard. An in-house uniaxial stretcher was used for the determination of material properties. Uniaxial tensile testing was performed below, within, and beyond physiological ranges of strain to gain an understanding of this elastic material under specific physiologic conditions. Calculations of the stress and strain are plotted in the principal direction.

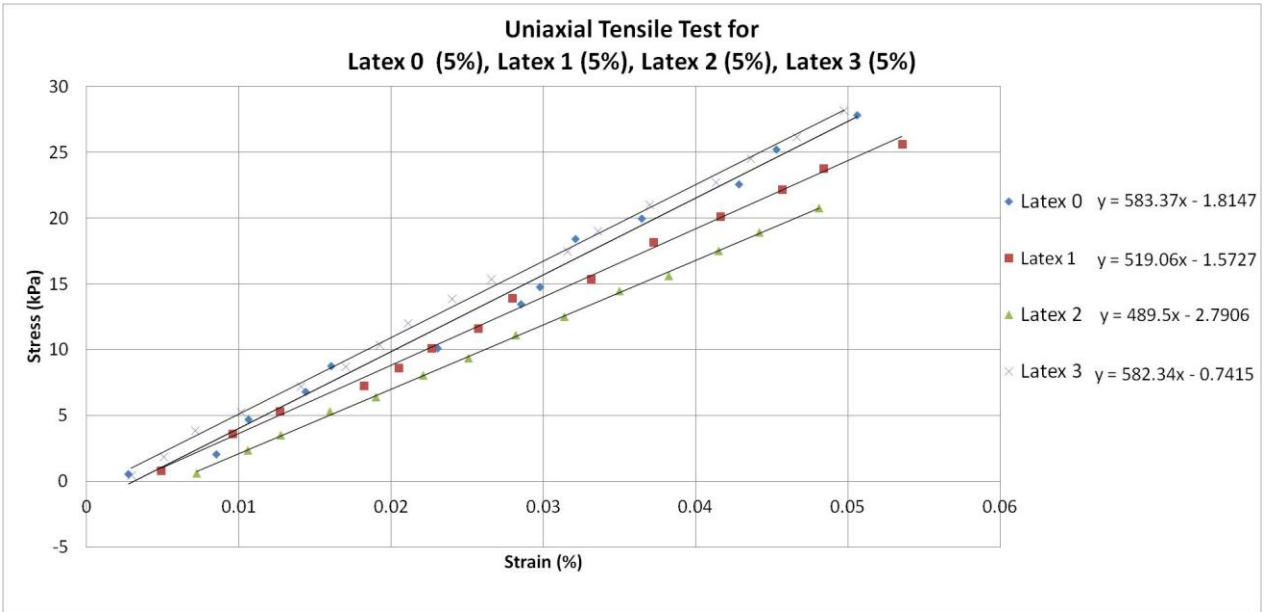

Figure 4.9. Stress and strain plot in various latex tubing using in-house uniaxial tensile testing. Wall thickness increases from latex 0 to latex 3. The slope is plotted relative to each latex tubing for comparison. Experiment performed December 18, 2009.

MECHANICAL TESTING

Cross-sectional area, initial length and loaded length of latex tubing were measured to determine Young's modulus of elasticity.

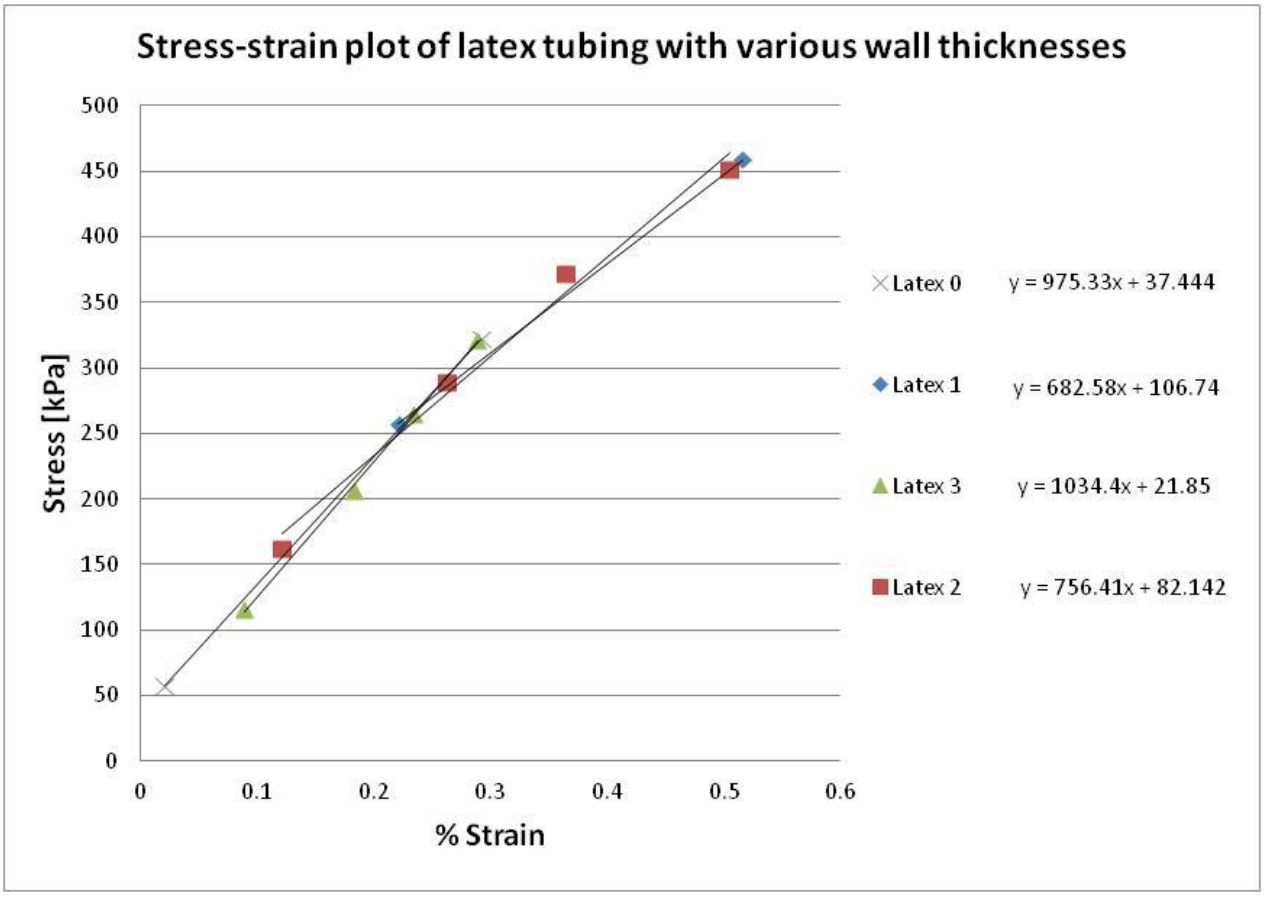

Figure 4.10. Stress and strain plot in various latex tubing using weights. Wall thickness increases from latex 0 to latex 3. The slope is plotted relative to each latex tubing for comparison. Experiment performed October 20, 2009.

ELECTRICAL NETWORK MODEL

Blood flow pulses and arterial pressure which result from the interaction of the arterial system and the heart have been a valuable resource in the assessment of cardiovascular disorder. Computer modeling of the arterial circulation presents a desirable option [32-40]. Models are utilized to assist the simplification and understanding of function in reality.

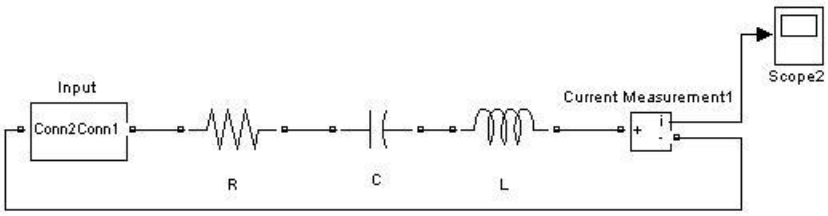

Figure 4.11. Electrical analog circuit model: current source in series circuit

UNDERDAMPED

The underdamped response is a decaying oscillation at frequency ω. The oscillation decays at a rate determined by the attenuation α.

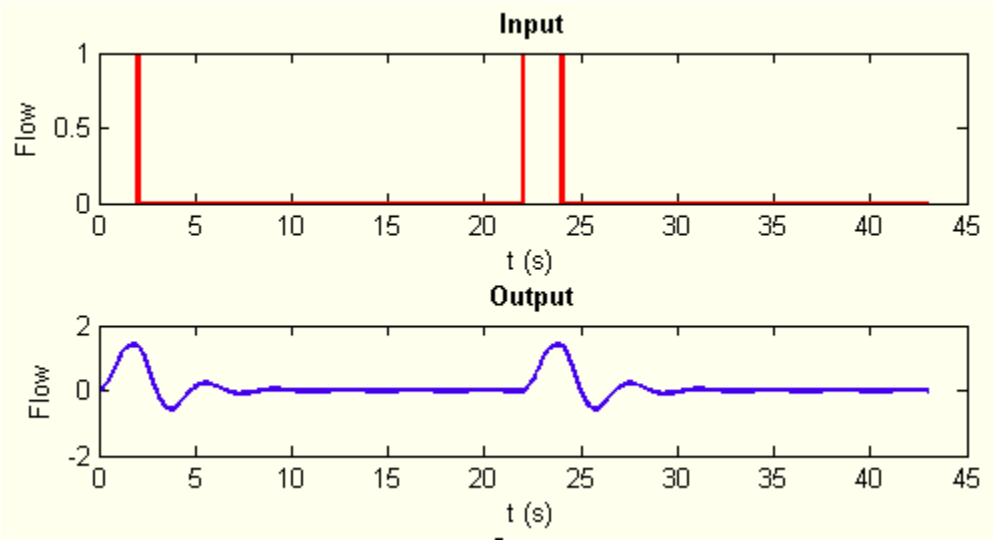

Figure 4.12. Input/output of current source in series circuit of electrical analog network model.

CHAPTER 5 DISCUSSION

IMAGING USING FLOW PHANTOM

PHASE CONTRAST METHOD

In the experiment performed on September 24, 2009 in Figure 4.2, from Latex1 to Latex4, the input square waveform is differentiated into double-peaks. The first peak is the mean velocity of the gear pump moving the water forward and the second peak is the mean velocity of the latex (elastic) tubing contracting and pushing the water forward. In other words, the first peak represents the mean velocity of primary blood flow post-systole through the aorta and the second peak represents the mean velocity of secondary blood flow post-diastole through the aorta. In Latex1, the first peak has a greater mean velocity than the second peak. This means that there is more reason for the water to move forward than the energy of the square waveform to be stored in the latex tubing. This translates to the inhibition for the secondary blood flow of the latex tubing to contribute to a greater blood flow than the primary blood flow of the gear pump. This could mean that the elastic latex tubing 1 has reached its “capacity” of being distended so the water will want to flow through the tubing. The second peak is the secondary flow when the latex tubing contracts and pushes the water from the energy storage of elastic tubing. As we look at the mean velocity waveform profiles, from Latex 2, 3, and 4, the first and second peaks of the mean velocity tends to level out. And in Latex4, the latex tubing with the greatest wall thickness has a second peak greater than that of the first peak. This means that the greater wall thickness latex tubing is capable of holding more energy than the lesser wall thickness latex tubing. The greater wall thickness latex tubing absorbs more of the energy when the input

square waveform passes through this test region than the lesser wall thickness latex tubing allowing the secondary flow to be greater than the primary flow.

In the experiment performed on October 5, 2009 in Figure 4.3, an obvious observation as duty cycle increases in a particular piece of latex tubing is that the overall mean velocity waveform profile increases. In addition, there seems to be additional peaks that form in correlation with the duty cycle increases. This could be because there is a distending/contracting of the latex tubing. There seems to be a slight time delay in the initiation of the first peak from latex 1 to latex 4. This could be that it takes a little longer time for the mean velocity to build up. We can see similar behavior in the second "highest" peak.

In the experiment performed on October 5, 2009 in Figure 4.4, an obvious observation as the amplitude of the input square wave changes is that the mean velocity waveform profiles changes as well. They have a direct relationship. In addition, the mean peak velocities are more distinct as the amplitude increases.

In the experiment performed on October 8, 2009 in Figure 4.5, an obvious observation as duty cycle increases in a particular piece of latex tubing is that the overall mean velocity waveform profile increases. There seems to be a slight time delay in the initiation of the first peak from latex 1 to latex 4. This could be that it takes a little longer

time for the mean velocity to build up. We can see similar behavior in the second "highest" peak. Moreover, there seems to be increasing backflow as duty cycle increases. This could be because there is an increase in pressure downstream and the design of the gear pump allows for small leakage back to the suction side. The design of the gear pump has fine clearances between the teeth and between the casing and the rotors, therefore a higher pressure downstream will likely increase the backflow of the fluid.

In the experiment performed on October 8, 2009 in Figure 4.6, an obvious observation as the amplitude of the input square wave changes is that the mean velocity waveform profiles changes as well. They have a direct relationship. In addition, the mean peak velocities are more distinct as the amplitude increases. Moreover, there seems to be increasing backflow amplitude increases. This could be because there is an increase in pressure downstream and the design of the gear pump allows for small leakage back to the suction side. The design of the gear pump has fine clearances between the teeth and between the casing and the rotors, therefore a higher pressure downstream will likely increase the backflow of the fluid.

In the experiment performed on October 8, 2009, in Figure 4.7, an obvious observation as duty cycle increases in a particular piece of latex tubing is that the overall mean velocity waveform profile increases. This could be because there is a higher discharge pressure. There seems to be a slight time delay in the initiation of the first peak from

latex 1 to latex 4. Moreover, there seems to be increasing backflow as duty cycle increases. This could be because there is an increase in pressure downstream and the design of the gear pump allows for small leakage back to the suction side. The design of the gear pump has fine clearances between the teeth and between the casing and the rotors, therefore a higher pressure downstream will likely increase the backflow of the fluid. Lastly, as duty cycle increases in a particular piece of latex tubing, the two peaks of the mean velocity waveform merges. At higher duty cycles, pressure tends to rise higher and the injection duration will also be higher. In other words, the tubing was able to distend and remain distended for the duration of the longer duty cycle, thus the output waveform nearly behaved like there were no wave reflection issues similar to rigid tubing.

In the experiment performed on October 8, 2009, in Figure 4.8, an obvious observation as the amplitude of the input square wave changes is that the mean velocity waveform profiles changes as well. They have a direct relationship. In addition, the mean peak velocities are more distinct as the amplitude increases. Moreover, there seems to be increasing backflow amplitude increases. This could be because there is an increase in pressure downstream and the design of the gear pump allows for small leakage back to the suction side. The design of the gear pump has fine clearances between the teeth and between the casing and the rotors, therefore a higher pressure downstream will likely increase the backflow of the fluid.

FOURIER VELOCITY ENCODING

In the experiment performed on November 10, 2009, in Table 4.1, an obvious observation as wall thickness increases in a particular piece of latex tubing is that the overall mean velocity waveform profile increases. This is in alignment with the distensibility equation:

$$D = 1 / (\rho V_{pw}^2) \qquad (7),$$

For the incompressible fluid in rigid tubing, pressure and flow changes would be instantly transmitted down the tubing, but for tubing with compliant walls, the input waveform distends the tubing and travels down at a finite velocity.

MECHANICAL TESTING

UNIAXIAL STRETCH TESTING

In the experiment performed on December 18, 2009, in Figure 4.9, the expectation is that the Young's modulus of elasticity for all the latex tubing to coincide since it was assumed that all material properties of the same material are the same, however, that was not the case. This could be because of the different equipment setup during the manufacturing extrusion process.

MECHANICAL TENSILE TESTING

Study of material properties of latex tubing utilized uniaxial stretch testing ranging from low to high strains.

The weight of the C-clamps was not ideal was after analysis of the data. The latex tubing was bearing too much load thus the stress-strain curve shows plastic deformation without truly knowing where the elastic region is located. The experiment's intention was to determine Young's modulus of the latex tubing, but experimental data displays plastic deformation or non-linear region.

The data shows that the Young's modulus was varying from the latex tubing with different wall thickness. This should not have been the case because Young's modulus is a material property. This conclusion was made with the assumption that the latex was the same material since they call came from McMaster Carr. According to the results, the assumption was wrong. The variation of Young's modulus from the various latex tubing could be because of the different equipment setup during the manufacturing extrusion process.

Knowing in the experiment, too high of a load was placed onto the latex tubing and that the data points collected shows only the plastic deformation region, the plots that are plotted in Figure 4.10 does not fully characterize the material property of the latex tubing.

Measurement of the cross-sectional area of the latex tubing was not taken post-stretching. Additionally, measurement of the length of the tubing was not taken place post-stretching. This could have checked if plastic deformation of material occurred.

However, the limited data points taken could have constructed an imperfect elastic portion of the linear region for determination of Young's modulus.

ELECTRICAL NETWORK MODEL

Parallel path is an electric circuit producing distinct or separate current flow through each division. Because current is analogous to flow velocity, a branch of latex tubing is unable to produce simultaneously two varying flow velocities unless there are separate and parallel tubes. Series path model represents the uniqueness of the tubing, both the capacitive compliant behavior as well as the resistive non-compliant behavior. Addition to the model is the inductor modeling flow inertia, however there is only one flow velocity at any given instant of time that is possible once the elements are connected in series.

COMPARE AND DISCUSSION

In imaging using the flow phantom as it applies to the phase contrast method, the screwy peaks show that there is a ton of compliance in the system and that in itself makes it difficult to do any of the analysis on it.

The first goal was to measure and compare compliance values and MRI estimates of various tubing using the 1D method. This was achieved and the data is displayed in Table 4.1. The key takeaway is as mean velocity increases, distensibility decreases in a particular piece of latex tubing.

The next goal was to design a model with segments that includes various compliance values and see if the 1D method can differentiate the different contributions to global compliance as a function of segment length. This was achieved and the data is

displayed in Table 4.1. The key takeaway is as wall thickness increases, distensibility decreases in a particular piece of latex tubing.

The last goal was to build an electrical analog network model using estimated values from experimental measurements. The electrical analog circuit model is displayed in Figure 4.11 and the Input/output in the series circuit is displayed in Figure 4.12. The key takeaway is that we were able to build an electrical analog network model that simulates the behavior found in imaging using the phase contrast method.

In summary, there is a direct relationship between the phase contrast method experiment and the electrical network model experiment in that they both produce an output that displays a double peak waveform when a square waveform is the input. Next, there is an interesting relationship between the phase contrast method and the Fourier-velocity encoding method in that as wall thickness increases, the mean velocity decreases in the phase contrast method and the pulse wave velocity increases in the Fourier- velocity encoding method. Lastly, the conclusions drawn from both the uniaxial stretch testing and mechanical tensile testing is that the Young's modulus is not the same across the latex tubing.

LIMITATIONS OF THE STUDY

Compliance, stiffness, and distensibility were not clearly defined prior to the experimentation and were used generically in the use of the term "compliance".

Initially, I believed that the distensibility equation

$$D = 1 / (\rho V_{pw}^2) \text{ (in Pa-1)} \qquad (7)$$

is the “definition” of distensibility. However, after clarification, the distensibility is a material property that can be determined from pulse wave velocity.

Compliance is defined as the change in volume divided by the change in pressure, but this is specific to the case of tubes with flow in them. During experimentation, the term “compliance” and “distensible” was generically used. For instance, the single pulse from the pump produced a waveform with two (2) peaks and the speculation is that the second peak was caused by the tube being able to distend and thus affect the waveform. If the system was made up of completely rigid tubing and there were no wave reflection issues, the waveform would be mostly unchanged from the input. With that said, the wave reflections at the connectors may be contributing to affect the single pulse input waveform.

So in essence, compliance, stiffness and distensibility are more general in how the terms were used and the lack of clarity is one important limitation to this study.

PROBLEMS OF THE SETUP

Our tubing may have too low of a compliance, so the pulse wave velocity was too high. Another issue is that our tubing was not surrounded by water, to damp vibrations and to also reduce artifacts that arise in MRI when you have an interface between air and

water. Experimenting with some thinner walled tubing and building an enclosure to surround the tubes are two (2) possible improvements for future work.

MECHANICAL TESTING

Uniaxial stretch testing

Strain %

Because the latex tubing specimen was loaded in the circumferential orientation, the preload affecting the latex tubing sample made determination of Young's modulus difficult especially if the curves plotted started in the latter part of the elastic region or plastic deformation region. The test specimen sheet tends to fold inward as if it was still a piece of tubing exhibiting a preload before starting tensile test. In future work, the latex tubing specimen should be loaded in the longitudinal orientation so that the preload affecting the latex tubing does not start the plotted curves in the latter part of the elastic region or plastic deformation region.

Wall Thickness Effects

Data shows an elastic deformation linear region but this data is questionable when larger wall thickness latex tubing is tensile tested. Thicker tubes tend to exert a larger force from wanting to fold back to the tube-form from the tested sheet-form. In future work, the latex tubing specimen should be loaded in the longitudinal orientation to reduce the tubing wanting to fold back to the tube-form.

Plastic Deformation

The plastic deformation region, nonlinear region, of the stress-strain curve was not included in the analysis of the Young's modulus. In future work, determination of material properties should be tested on tensile testing equipment.

Retesting

Retesting using same piece of latex specimen after plastic deformation is not reliable for the measurement of elastic modulus. After initial stretch testing, latex may have deformed plastically, therefore when stretching the second time, the change in strain is longer calculated from the original length. In future work, the latex specimen must be only tested once.

FUTURE WORK AND POSSIBLE IMPROVEMENTS

In the fluid phantom setup, the fluid phantom model does not characterize physiological behavior of the aorta well enough to fully understand and validate these MRI algorithms. The peaks show that there is a ton of compliance in the system and that in itself makes it difficult to do any of the analysis on it. Future work includes changing out the garden hose and replacing it with rigid tubing. I believe that the garden hose consists of an inner elastic wall. An elastic region where the fluid flows through would contribute to changes in the shape of the input square wave before the square wave flows through the test region where the latex tubing is in place. Lastly, the connectors may be playing a part of in affecting the waveform. In future work, a different design to the setup where

it does not require connectors may reduce any effects to the input waveform prior to the latex test specimen.

In mechanical testing, the determination of material properties should be tested on tensile testing equipment. Moreover, retesting using the same piece of latex specimen is not reliable since the latex may deform plastically. In future work, the latex specimen must be only tested once.

In the material selection to characterize the patient aorta, latex tubing may not have been the most appropriate option, but this was the cheapest material at the time that came closest to the elastic modulus of the aorta and was readily available.

REFERENCE

1. Firmin, D.N., et al., *Magnetic resonance imaging: a method for the assessment of changes in vascular structure and function.* J Hum Hypertens, 1991. **5 Suppl 1**: p. 31-40.
2. Metafratzi, Z.M., et al., *The clinical significance of aortic compliance and its assessment with magnetic resonance imaging.* J Cardiovasc Magn Reson, 2002. **4**(4): p. 481-91.
3. Hardy, C.J., *Assessment of Arterial Elasticity by Cardiovascular MRI*, in *Cardiovascular Magnetic Resonance Imaging*. 2008. p. 695-710.
4. Roach, M.R. and A.C. Burton, *The reason for the shape of the distensibility curves of arteries.* Can J Biochem Physiol, 1957. **35**(8): p. 681-90.
5. Chen, C.W., Y.W. Shau, and C.P. Wu, *Analog transmission line model for simulation of systemic circulation.* IEEE Trans Biomed Eng, 1997. **44**(1): p. 90-4.
6. Stergiopulos, N., D.F. Young, and T.R. Rogge, *Computer simulation of arterial flow with applications to arterial and aortic stenoses.* J Biomech, 1992. **25**(12): p. 1477-88.
7. Viedma, A., C. Jimenez-Ortiz, and V. Marco, *Extended Willis circle model to explain clinical observations in periorbital arterial flow.* J Biomech, 1997. **30**(3): p. 265-72.
8. Mates, R.E., F.J. Klocke, and J.M. Canty, Jr., *Coronary capacitance.* Prog Cardiovasc Dis, 1988. **31**(1): p. 1-15.
9. Nichols, W.W., et al., *Ventricular/vascular interaction in patients with mild systemic hypertension and normal peripheral resistance.* Circulation, 1986. **74**(3): p. 455-62.
10. Ting, C.T., et al., *Arterial hemodynamics in human hypertension.* J Clin Invest, 1986. **78**(6): p. 1462-71.
11. Wilcken, D.E., et al., *Effects of Alterations in Aortic Impedance on the Performance of the Ventricles.* Circ Res, 1964. **14**: p. 283-93.
12. Urschel, C.W., et al., *Effects of decreased aortic compliance on performance of the left ventricle.* Am J Physiol, 1968. **214**(2): p. 298-304.
13. Franklin, S.S., et al., *Is pulse pressure useful in predicting risk for coronary heart Disease? The Framingham heart study.* Circulation, 1999. **100**(4): p. 354-60.
14. Learoyd, B.M. and M.G. Taylor, *Alterations with age in the viscoelastic properties of human arterial walls.* Circ Res, 1966. **18**(3): p. 278-92.
15. Mohiaddin, R.H., et al., *Regional aortic compliance studied by magnetic resonance imaging: the effects of age, training, and coronary artery disease.* Br Heart J, 1989. **62**(2): p. 90-6.
16. Mohiaddin, R.H., D.N. Firmin, and D.B. Longmore, *Age-related changes of human aortic flow wave velocity measured noninvasively by magnetic resonance imaging.* J Appl Physiol, 1993. **74**(1): p. 492-7.
17. Bogren, H.G., et al., *The function of the aorta in ischemic heart disease: a magnetic resonance and angiographic study of aortic compliance and blood flow patterns.* Am Heart J, 1989. **118**(2): p. 234-47.
18. Matsumoto, Y., et al., *Evaluation of aortic distensibility in patients with coronary artery disease by use of cine magnetic resonance.* Angiology, 1996. **47**(2): p. 149-55.
19. Di Renzi, P., et al., *[Evaluation of aortic distensibility using cine-MR before and after antihypertensive treatment with calcium antagonists and ACE-inhibitors].* Cardiologia, 1993. **38**(12): p. 779-84.
20. Honda, T., et al., *Evaluation of aortic distensibility in patients with essential hypertension by using cine magnetic resonance imaging.* Angiology, 1994. **45**(3): p. 207-12.
21. Resnick, L.M., et al., *Direct magnetic resonance determination of aortic distensibility in essential hypertension: relation to age, abdominal visceral fat, and in situ intracellular free magnesium.* Hypertension, 1997. **30**(3 Pt 2): p. 654-9.

22. Toikka, J.O., et al., *Decreased large artery distensibility in borderline hypertension is related to increased in vivo low-density lipoprotein oxidation.* Scand J Clin Lab Invest, 2002. **62**(4): p. 301-6.
23. Bogren, H.G., et al., *Pulmonary artery distensibility and blood flow patterns: a magnetic resonance study of normal subjects and of patients with pulmonary arterial hypertension.* Am Heart J, 1989. **118**(5 Pt 1): p. 990-9.
24. Rerkpattanapipat, P., et al., *Relation of aortic distensibility determined by magnetic resonance imaging in patients > or =60 years of age to systolic heart failure and exercise capacity.* Am J Cardiol, 2002. **90**(11): p. 1221-5.
25. Hundley, W.G., et al., *Cardiac cycle-dependent changes in aortic area and distensibility are reduced in older patients with isolated diastolic heart failure and correlate with exercise intolerance.* J Am Coll Cardiol, 2001. **38**(3): p. 796-802.
26. Savolainen, A., et al., *Aortic distensibility in children with the Marfan syndrome.* Am J Cardiol, 1992. **70**(6): p. 691-3.
27. Adams, J.N., et al., *Aortic distensibility and stiffness index measured by magnetic resonance imaging in patients with Marfan's syndrome.* Br Heart J, 1995. **73**(3): p. 265-9.
28. Groenink, M., et al., *Changes in aortic distensibility and pulse wave velocity assessed with magnetic resonance imaging following beta-blocker therapy in the Marfan syndrome.* Am J Cardiol, 1998. **82**(2): p. 203-8.
29. Fattori, R., et al., *Magnetic resonance imaging evaluation of aortic elastic properties as early expression of Marfan syndrome.* J Cardiovasc Magn Reson, 2000. **2**(4): p. 251-6.
30. Nollen, G.J., et al., *Aortic stiffness and diameter predict progressive aortic dilatation in patients with Marfan syndrome.* Eur Heart J, 2004. **25**(13): p. 1146-52.
31. Khau Van Kien, P., et al., *Mapping of familial thoracic aortic aneurysm/dissection with patent ductus arteriosus to 16p12.2-p13.13.* Circulation, 2005. **112**(2): p. 200-6.
32. Snyder, M.F., V.C. Rideout, and R.J. Hillestad, *Computer modeling of the human systemic arterial tree.* J Biomech, 1968. **1**(4): p. 341-53.
33. Westerhof, N., et al., *Analog studies of the human systemic arterial tree.* J Biomech, 1969. **2**(2): p. 121-43.
34. Anliker, M., R.L. Rockwell, and E. Ogden, *Nonlinear analysis of flow pulses and shock waves in arteries.* Zeitschrift für Angewandte Mathematik und Physik (ZAMP), 1971. **22**(3): p. 563-581.
35. Schaaf, B.W. and P.H. Abbrecht, *Digital computer simulation of human systemic arterial pulse wave transmission: a nonlinear model.* J Biomech, 1972. **5**(4): p. 345-64.
36. Wemple, R.R. and L.F. Mockros, *Pressure and flow in the systemic arterial system.* J Biomech, 1972. **5**(6): p. 629-41.
37. Raines, J.K., M.Y. Jaffrin, and A.H. Shapiro, *A computer simulation of arterial dynamics in the human leg.* J Biomech, 1974. **7**(1): p. 77-91.
38. Avolio, A.P., *Multi-branched model of the human arterial system.* Med Biol Eng Comput, 1980. **18**(6): p. 709-18.
39. Porenta, G., D.F. Young, and T.R. Rogge, *A finite-element model of blood flow in arteries including taper, branches, and obstructions.* J Biomech Eng, 1986. **108**(2): p. 161-7.
40. Balar, S.D., T.R. Rogge, and D.F. Young, *Computer simulation of blood flow in the human arm.* J Biomech, 1989. **22**(6-7): p. 691-7.
41. Dart, A.M., et al., *Aortic distensibility in patients with isolated hypercholesterolaemia, coronary artery disease, or cardiac transplant.* Lancet, 1991. **338**(8762): p. 270-3.
42. Merillon, J.P., et al., *Evaluation of the elasticity and characteristic impedance of the ascending aorta in man.* Cardiovasc Res, 1978. **12**(7): p. 401-6.
43. Dahan, M., et al., *Doppler echocardiographic study of the consequences of aging and hypertension on the left ventricle and aorta.* Eur Heart J, 1990. **11 Suppl G**: p. 39-45.

44. Kelly, R., et al., *Noninvasive determination of age-related changes in the human arterial pulse.* Circulation, 1989. **80**(6): p. 1652-9.
45. Vaitkevicius, P.V., et al., *Effects of age and aerobic capacity on arterial stiffness in healthy adults.* Circulation, 1993. **88**(4 Pt 1): p. 1456-62.
46. Ting, C.T., et al., *Regional pulse wave velocities in hypertensive and normotensive humans.* Cardiovasc Res, 1990. **24**(11): p. 865-72.
47. FerrÃ¡ndez, A., et al., *Computational Models of Blood Flow in the Circle of Willis.* Computer Methods in Biomechanics and Biomedical Engineering, 2001. **4**(1): p. 1 - 26.
48. Stokholm, R., et al., *Determination of wall shear rate in the human carotid artery by magnetic resonance techniques.* Eur J Vasc Endovasc Surg, 2000. **20**(5): p. 427-33.
49. Fayad, Z.A. and V. Fuster, *The human high-risk plaque and its detection by magnetic resonance imaging.* Am J Cardiol, 2001. **88**(2A): p. 42E-45E.
50. Yuan, C., et al., *Carotid atherosclerotic plaque: noninvasive MR characterization and identification of vulnerable lesions.* Radiology, 2001. **221**(2): p. 285-99.
51. Wedding, K.L., et al., *Measurement of vessel wall strain using cine phase contrast MRI.* J Magn Reson Imaging, 2002. **15**(4): p. 418-28.
52. Long, Q., et al., *Reconstruction of blood flow patterns in a human carotid bifurcation: a combined CFD and MRI study.* J Magn Reson Imaging, 2000. **11**(3): p. 299-311.
53. Steinman, D.A., et al., *Reconstruction of carotid bifurcation hemodynamics and wall thickness using computational fluid dynamics and MRI.* Magn Reson Med, 2002. **47**(1): p. 149-59.
54. Moore, S.M., et al., *One-dimensional and three-dimensional models of cerebrovascular flow.* J Biomech Eng, 2005. **127**(3): p. 440-9.
55. Bock, M., et al., *Pulsewave velocity measurement using a new real-time MR-method.* Magn Reson Imaging, 1995. **13**(1): p. 21-9.
56. Caro, C.G., *The Mechanics of the circulation / C. G. Caro ... [et al.]*. 1978, Oxford ; New York :: Oxford University Press. xiv, 527 p. :.
57. Chien, D., et al., *High resolution cine MRI of vessel distension.* J Comput Assist Tomogr, 1994. **18**(4): p. 576-80.
58. Karamanoglu, M., et al., *An analysis of the relationship between central aortic and peripheral upper limb pressure waves in man.* Eur Heart J, 1993. **14**(2): p. 160-7.
59. Fahrig, R., et al., *A three-dimensional cerebrovascular flow phantom.* Med Phys, 1999. **26**(8): p. 1589-99.
60. Matthews, P.B., et al., *Comparison of porcine pulmonary and aortic root material properties.* Ann Thorac Surg. **89**(6): p. 1981-8.
61. Bergel, D.H., *The dynamic elastic properties of the arterial wall.* J Physiol, 1961. **156**(3): p. 458-69.
62. Beyar, R., et al., *Interaction between cardiac chambers and thoracic pressure in intact circulation.* Am J Physiol, 1987. **253**(5 Pt 2): p. H1240-52.
63. Burattini, R. and G. Gnudi, *Computer identification of models for the arterial tree input impedance: comparison between two new simple models and first experimental results.* Med Biol Eng Comput, 1982. **20**(2): p. 134-44.
64. Liu, Z.R., F. Shen, and F.C. Yin, *Impedance of arterial system simulated by viscoelastic t tubes terminated in windkessels.* Am J Physiol, 1989. **256**(4 Pt 2): p. H1087-99.
65. Nichols, W.W., et al., *Input impedance of the systemic circulation in man.* Circ Res, 1977. **40**(5): p. 451-8.
66. Toy, S.M., J. Melbin, and A. Noordergraaf, *Reduced models of arterial systems.* IEEE Trans Biomed Eng, 1985. **32**(2): p. 174-6.

67. John, L.R., *Forward electrical transmission line model of the human arterial system.* Med Biol Eng Comput, 2004. **42**(3): p. 312-21.
68. Frank, O., *Die theorie der pulswellen*. Vol. 85. 1926: Z Biol.
69. Milnor, W.R., *Hemodynamics*. 1989, Baltimore, Maryland: Williams and Wilkins.
70. Greenwald, S.E., *Pulse pressure and arterial elasticity.* QJM, 2002. **95**(2): p. 107-12.
71. Frank, O., *Die Grundform des arteriellen Pulses*. Vol. 37. 1899: Z Biol.
72. Westerhof, N., G. Elzinga, and P. Sipkema, *An artificial arterial system for pumping hearts.* J Appl Physiol, 1971. **31**(5): p. 776-81.
73. Burattini, R., G.G. Knowlen, and K.B. Campbell, *Two arterial effective reflecting sites may appear as one to the heart.* Circ Res, 1991. **68**(1): p. 85-99.
74. O'Rourke, M.F., *Pressure and flow waves in systemic arteries and the anatomical design of the arterial system.* J Appl Physiol, 1967. **23**(2): p. 139-49.
75. Wetterer E, K.T., *Grundlagen der Dynamik des Arterienpulses*. 1968, Springer, Berlin.
76. O'Rourke, M.F. and A.P. Avolio, *Pulsatile flow and pressure in human systemic arteries. Studies in man and in a multibranched model of the human systemic arterial tree.* Circ Res, 1980. **46**(3): p. 363-72.
77. Westerhof, N., J.W. Lankhaar, and B.E. Westerhof, *The arterial Windkessel.* Med Biol Eng Comput, 2009. **47**(2): p. 131-41.
78. Simon, A.C., et al., *An evaluation of large arteries compliance in man.* Am J Physiol, 1979. **237**(5): p. H550-4.
79. Randall, O.S., G.C. van den Bos, and N. Westerhof, *Systemic compliance: does it play a role in the genesis of essential hypertension?* Cardiovasc Res, 1984. **18**(8): p. 455-62.
80. Benetos, A., et al., *Pulse pressure: a predictor of long-term cardiovascular mortality in a French male population.* Hypertension, 1997. **30**(6): p. 1410-5.
81. Mitchell, G.F., et al., *Sphygmomanometrically determined pulse pressure is a powerful independent predictor of recurrent events after myocardial infarction in patients with impaired left ventricular function. SAVE investigators. Survival and Ventricular Enlargement.* Circulation, 1997. **96**(12): p. 4254-60.
82. Snyder WS, C.M., Nasset ES, Karhausen LR, Howells GP, Tipton IH, *Report of the Task Group on Reference Man*. 1975, Oxford, United Kingdom: Pergamon Press.
83. Paz, R., R.H. Mohiaddin, and D.B. Longmore, *Magnetic resonance assessment of the pulmonary arterial trunk anatomy, flow, pulsatility and distensibility.* Eur Heart J, 1993. **14**(11): p. 1524-30.
84. Buonocore, M.H. and H. Bogren, *Optimized pulse sequences for magnetic resonance measurement of aortic cross sectional areas.* Magn Reson Imaging, 1991. **9**(3): p. 435-47.
85. Forbat, S.M., et al., *Measurement of regional aortic compliance by MR imaging: a study of reproducibility.* J Magn Reson Imaging, 1995. **5**(6): p. 635-9.
86. Krug, R., J.M. Boese, and L.R. Schad, *Determination of aortic compliance from magnetic resonance images using an automatic active contour model.* Phys Med Biol, 2003. **48**(15): p. 2391-404.
87. Crowe, L.A., et al., *Volume-selective 3D turbo spin echo imaging for vascular wall imaging and distensibility measurement.* J Magn Reson Imaging, 2003. **17**(5): p. 572-80.
88. Boese, J.M., et al., *Estimation of aortic compliance using magnetic resonance pulse wave velocity measurement.* Phys Med Biol, 2000. **45**(6): p. 1703-13.
89. Grotenhuis HB, W.J., Doornbos J, et al., *In-plane pulse wave velocity with MRI in ischemic heart disease: validation of a new technique.* Journal of Cardiovascular Magnetic Resonance, 2005(7): p. 120-121.
90. Macgowan, C.K., R.M. Henkelman, and M.L. Wood, *Pulse-wave velocity measured in one heartbeat using MR tagging.* Magn Reson Med, 2002. **48**(1): p. 115-21.

91. Shao, X., D.Y. Fei, and K.A. Kraft, *Rapid measurement of pulse wave velocity via multisite flow displacement.* Magn Reson Med, 2004. **52**(6): p. 1351-7.
92. PAULY, et al., *A k-space analysis of small-tip-angle excitation*. Vol. 81. 1989, Orlando, FL, ETATS-UNIS: Academic Press. 14.
93. Hardy, C.J. and H.E. Cline, *Broadband nuclear magnetic resonance pulses with two-dimensional spatial selectivity.* Journal of Applied Physics, 1989. **66**(4): p. 1513-1516.
94. Redpath, T.W., et al., *A new method of NMR flow imaging.* Phys Med Biol, 1984. **29**(7): p. 891-5.
95. Feinberg, D.A., et al., *Magnetic resonance imaging the velocity vector components of fluid flow.* Magn Reson Med, 1985. **2**(6): p. 555-66.
96. Dumoulin, C.L., D.J. Doorly, and C.G. Caro, *Quantitative measurement of velocity at multiple positions using comb excitation and Fourier velocity encoding.* Magn Reson Med, 1993. **29**(1): p. 44-52.
97. Hardy, C.J., et al., *Pencil excitation with interleaved fourier velocity encoding: NMR measurement of aortic distensibility.* Magn Reson Med, 1996. **35**(6): p. 814-9.
98. Hardy, C.J., et al., *A one-dimensional velocity technique for NMR measurement of aortic distensibility.* Magn Reson Med, 1994. **31**(5): p. 513-20.
99. Kraft, K.A., et al., *Proceedings of 13th Meeting of International Society for Magnetic Resonance in Medicine.* 2005: p. 601.
100. Urchuk, S.N. and D.B. Plewes, *A velocity correlation method for measuring vascular compliance using MR imaging.* J Magn Reson Imaging, 1995. **5**(6): p. 628-34.
101. Urchuk, S.N., S.E. Fremes, and D.B. Plewes, *In vivo validation of MR pulse pressure measurement in an aortic flow model: preliminary results.* Magn Reson Med, 1997. **38**(2): p. 215-23.
102. Vulliemoz, S., N. Stergiopulos, and R. Meuli, *Estimation of local aortic elastic properties with MRI.* Magn Reson Med, 2002. **47**(4): p. 649-54.
103. Auseon A, G.A., Tran T, Hardy CJ, Raman SV, *Aortic anatomy and physiology with magnetic resonance aortic wall imaging and pulse wave velocity measurement.* Journal of Cardiovascular Magnetic Resonance, 2005(7): p. 130-131.
104. Groenink, M., et al., *Biophysical properties of the normal-sized aorta in patients with Marfan syndrome: evaluation with MR flow mapping.* Radiology, 2001. **219**(2): p. 535-40.
105. Oosterhof, T., et al., *Comparison of aortic stiffness in patients with juvenile forms of ascending aortic dilatation with versus without Marfan's syndrome.* Am J Cardiol, 2005. **95**(8): p. 996-8.
106. Arita, M., H. Kasegawa, and M. Umezu, *Development of In-Vitro Evaluation System for Annuloplasty Rings.* Asian Cardiovascular and Thoracic Annals, 2001. **9**(1): p. 14-18.
107. John, L.R., *Forward electrical transmission line model of the human arterial system.* Medical and Biological Engineering and Computing, 2004. **42**(3): p. 312-321.